Retrievals of high latitude surface emissivity across the infrared from high altitude aircraft flights

Jonathan E. Murray[1], Helen E. Brindley[1,2], Stuart Fox[3], Christophe Bellisario[2*], Juliet C Pickering[1], Cathryn Fox[3], Chawn Harlow[3], Maureen Smith[4], Doug Anderson[4], Xianglei Huang[5], Xiuhong Chen[5], Alan Last[1] and Richard Bantges[1,2]

[1]Space and Atmospheric Physics Group, Imperial College London, UK. [2]National Centre for Earth Observation, Imperial College London, UK. [3]Met Office, Exeter, UK. [4]Facility for Airborne Atmospheric Measurements (FAAM), Cranfield, UK. [5]Department of Climate and Space Sciences and Engineering, University of Michigan, Ann Arbor, MI, USA. * Now at DOTA, ONERA, France.

Corresponding author: Jonathan E. Murray (j.murray@imperial.ac.uk), Helen E. Brindley (h.brindley@imperial.ac.uk)

Key Points:

- Retrievals of surface emissivity and temperature across the thermal infrared from high altitude aircraft measurements are reported

- Retrieved far infrared emissivities are significantly less than unity, showing consistency with near-surface retrievals in the same flight

- This emissivity and surface temperature retrieval methodology is applicable to proposed satellite instruments covering the thermal infrared

Abstract

We present retrievals of infrared spectral surface emissivities spanning the far and mid infrared from aircraft observations over Greenland, taken at an altitude of 9.2 km above sea level. We describe the flight campaign, available measurements and the retrieval method. The principal barriers to reducing uncertainty in the emissivity retrievals are found to be instrumental noise and our ability to simultaneously retrieve the underlying surface temperature. However, our results indicate that using the instrumentation available to us it is possible to retrieve emissivities from altitude with an uncertainty of ∼ 0.02 or better across much of the infrared. They confirm that the far-infrared emissivity of snow and ice surfaces can depart substantially from unity, reaching values as low as 0.9 between 400-450 cm^{-1}. They also show good consistency with retrievals from the same flight made from near-surface observations giving confidence in the methodology used and the results obtained for this more challenging viewing configuration. To the best of our knowledge, this is the first time that far-infrared surface emissivity has been retrieved from altitude and demonstrates that the methodology has the potential to be extended to planned satellite far-infrared missions.

1 Introduction

The far infrared (FIR) defined here as wavelengths, $\lambda > 15$ μm, or equivalently wavenumbers, $\nu < 667$ cm^{-1} contributes around 50 % to the total outgoing longwave (infrared) radiation to space in the global mean. Typically, even in clear-sky conditions, strong absorption by water vapour means that at these wavelengths the surface is obscured when viewed from any significant altitude (Harries *et al*., 2008). However, the cold, dry conditions often encountered at high latitudes simultaneously shift the peak of the Planck function to longer wavelengths and see semi-transparent micro-windows in the FIR open up, allowing surface emission to propagate further through the atmosphere. Under these conditions it is possible to observe FIR surface emission from space. Knowledge of the FIR surface emissivity is therefore required to accurately model the Earth's energy budget in these regions.

Chen et al. (2014) first points out the importance of FIR surface emissivity in influencing polar radiation budgets using offline radiative transfer calculations and theoretical modeling of snow surface spectral emissivity in the FIR. Feldman *et al*. (2014) further illustrates the importance of the FIR surface emissivity in the Community Earth System Model (CESM) and introduces the concept of an 'ice-emissivity' feedback, whereby the emissivity changes induced by melting sea-ice accelerate subsequent surface warming. Further studies with CESM reinforce the role of infrared surface emission of snow and ice surfaces in influencing polar climate: Kuo *et al*. (2018) show how the adoption of spectrally varying surface emissivities significantly reduces a persistent warm wintertime bias in Arctic surface temperature, while Huang *et al*. (2018) note significant changes in sea-ice fraction and that the sea ice-emissivity feedback, although small, depends critically on assumptions made concerning the surface geometry and properties of the overlying snow. However, while the mid infrared (MIR: $15 > \lambda > 4$ μm) surface emissivities used in these studies are based on observations, the FIR values are based on theoretical predictions and have yet to be directly validated. The inhibiting factor is a lack of suitable spectrally resolved observations across the FIR from which the surface emissivity can be inferred.

Bellisario *et al*., (2017, hereafter B17), exploited near-surface observations from an aircraft flight over Greenland to obtain, to the best of our knowledge, the first observationally based estimates

of FIR surface emissivity. The goal of this paper is to investigate whether surface emissivities spanning the FIR and MIR can also be retrieved from measurements made from the same flight but from the aircraft transit within the upper troposphere/lower stratosphere. A key test is whether the values retrieved from the upper level observations show consistency with the near surface retrievals. The findings have direct relevance for two upcoming FIR satellite missions: NASA's Polar Radiant Energy in the Far Infra Red Experiment (PREFIRE) and ESA's Far-infrared Outgoing Radiation Understanding and Monitoring (FORUM) mission (Palchetti *et al.*, 2020, Palchetti *et al.*, 2016). Given that both aim to infer Arctic and, potentially, Antarctic surface emissivities in the FIR, the analyses performed here provide a useful indication of what can be achieved, taking into consideration the uncertainties in both the measured radiances and the atmospheric state.

The paper is organised as follows: section 2 outlines the emissivity retrieval methodology. Section 3 describes the flight campaign and data sets used to retrieve the spectral emissivity across the infrared. In section 4 the emissivities derived in this study are presented and compared to those obtained in B17 to assess the consistency between values obtained at low and high altitudes. The sources of uncertainty in the retrievals are considered and discussed, before drawing conclusions in section 5.

2. Emissivity Retrieval Methodology

Under clear-sky conditions upwelling infrared radiance measurements, $L_{\nu}{}^{\uparrow}{}_{aircraft}$, acquired at the aircraft during the high altitude runs over the Greenland ice sheet can be described by:

$$L_{\nu}{}^{\uparrow}{}_{aircraft} = \tau_{\nu}\varepsilon_{\nu}B_{\nu}(T_S) + \tau_{\nu}(1 - \varepsilon_{\nu})L_{\nu}^{\downarrow} + L_{\nu}^{\uparrow} \qquad (1)$$

The first term on the right-hand side is the direct contribution from surface emission, where τ_{ν} is the atmospheric transmission between the surface and the aircraft and $\varepsilon_{\nu}B_{\nu}(T_s)$ is the surface emission, the product of the surface emissivity and the Planck emission from a surface emitting at temperature T_s. The second term is the contribution from the downwelling radiance at the surface, $L_{\nu}^{\downarrow}$, which is reflected and transmitted back through the atmosphere to the aircraft. The final term, $L_{\nu}^{\uparrow}$, is the upwelling atmospheric emission from the layer between the surface and aircraft.

Following the rationale presented in B17 we assume Lambertian surface behaviour and approximate the angularly-integrated downwelling radiance by the effective radiance, $L_{\nu,eff}^{\downarrow}$, calculated at a single incidence angle of 55°. Rearranging 1 then gives:

$$\varepsilon_{\nu} = \frac{L_{\nu}{}^{\uparrow}{}_{aircraft} - \tau_{\nu}L_{\nu,eff}^{\downarrow} - L_{\nu}^{\uparrow}}{\tau_{\nu}\left(B_{\nu}(T_S) - L_{\nu,eff}^{\downarrow}\right)} \qquad (2)$$

Equations 1 and 2 highlight two of the main challenges associated with retrieving surface emissivity from remotely measured radiances: (a) the difficulty in separating the influence of surface temperature and emissivity on the upwelling radiation from the surface and (b) the contaminating effect of the overlying atmosphere on the actual measured signal, $L_{v\ aircraft}^{\uparrow}$, (e.g. Li *et al*. 2013). Even if the state of the atmosphere is perfectly known, allowing (b) to be mitigated, the retrieval of emissivity requires a simultaneous estimate of T_s.

B17 took advantage of such a simultaneous technique, developed by Newman *et al*. (2005) for MIR measurements, to obtain an estimate of T_s. The approach, which assumes that surface emissivity varies smoothly with wavenumber across the spectrum, was designed for, and is best applied to, near surface radiances due to issue (b) identified above. In contrast, while Knuteson *et al*. (2004) make a similar underlying assumption, they describe a technique to separate 'effective' surface emissivity and temperature using a smaller range of MIR hyperspectral radiances measured from aircraft at high altitude. The term 'effective' is introduced to encompass the impact of inhomogeneities in the surface type over the aircraft footprint on the retrieved temperature and emissivity values. In their approach they select a limited spectral region which includes both atmospheric absorption lines and micro-windows and successively solve equation 2 for emissivity over a range of different surface temperatures. The effective surface temperature, T_{se}, is then defined as:

$$T_{se} = T_{se}^0 \ni \varepsilon_v(T_{se}^0) = \frac{min}{T_{se}'}\left\{||\varepsilon_v(T_{se}')||_{[v_1,v_2]}^{1/2}\right\} \quad (3)$$

which is the temperature that minimises the spectral standard deviation in the retrieved surface emissivity over the given spectral range. This temperature can then be used in equation 2 to derive the emissivity across the remainder of the spectrum. Note that if the scene is homogeneous over the instrument footprint the retrieved values relax to the true surface temperature and emissivity values. Knuteson *et al*. (2004) select the region 960-990 cm^{-1} for their analysis. This has minimal water vapour line contamination but does include the weak R-branch of the symmetric stretch mode to the asymmetric stretch mode of CO_2, commonly exploited as lasing transitions. We make a similar selection here but to help to understand the limitations of the method we also include an additional range covering the CO_2 P-branch, between 930 cm^{-1} and 960 cm^{-1}.

We note that given the spectral range and resolution of the aircraft spectra employed here we could simultaneously retrieve multiple targets such as surface temperature, surface emissivity, atmospheric temperature and water vapour profiles. Our motivation for choosing a sequential approach, retrieving first the surface temperature and then the emissivity separately, is primarily that it allows a cleaner route to evaluate the impact of the uncertainty associated with each variable that influences the overall error budget. A second motivation is that it is more consistent with the approach of Bellisario et al. (2017), with whose results we make comparisons. A sequential approach may also prove advantageous in cases where the surface temperature is better constrained by retrievals from independent measurements. For example, FORUM based retrievals of far-infrared emissivity may benefit from thermodynamic state retrievals from the Infrared Atmospheric Sounding Interferometer Next Generation (IASI-NG),

with which it will fly in loose formation, given that the goal noise equivalent spectral radiance for IASI-NG is smaller.

3 The radiation instrumentation, Greenland flight and ancillary data

The emissivity retrievals utilise measurements from the Facility for Airborne Atmospheric Measurements (FAAM) UK's BAe 146-301 aircraft taken during the Cirrus Coupled Cloud Radiation Experiment/Cold-air Outbreak and Sub-millimetre Ice Cloud Study (CIRCCREX/COSMICS) projects. Specifically, we make use of the spectrally resolved radiative measurements of the Tropospheric Airborne Fourier Transform Spectrometer (TAFTS, Canas *et al*., 1997) and the Airborne Research Interferometer Evaluation System (ARIES, Wilson *et al*., 1999), taken from an altitude of 9.2 km above sea-level. More detailed information concerning the operation of the two radiometers can be found in B17 but for clarity we repeat some information pertinent to the high level measurements analysed here.

3.1 The TAFTS instrument

TAFTS is a Martin-Puplett polarising interferometer (Martin *et al*., 1969) covering the spectral range of $80 – 600$ cm^{-1} and has been deployed in numerous airborne field campaigns (e.g. Cox et al., 2010, Green et al., 2012, Bantges et al., 2020). TAFTS uses two sets of liquid helium cooled detectors. The "long-wave" detector is a GeGa photoconductor covering 80-300 cm^{-1} and the "short-wave" detector is a SiSb photoconductor covering 330 - 600 cm^{-1} at a nominal resolution of 0.12 cm^{-1}. The field of view is +/-0.8^{o} and for the high level observations described in this paper the aircraft-to-surface distance is approximately 6 km, yielding an instantaneous footprint of 170 m. The acquisition time for a single nadir scan is approximately 2 s, with a 0.5 s turn around. The aircraft was travelling at about 140 m s^{-1} so that the 170 m footprint was smeared along the track by 280 m for individual scans, i.e. a ground footprint of 170 m x 350 m. A data acquisition cycle for TAFTS consists of internal calibration and external nadir and zenith views. A single cycle takes a little over 4 minutes during which approximately 50 seconds is dedicated to nadir scans of the upwelling radiance field. The high level transit over Greenland took about 40 minutes resulting in 10 sets of 18 nadir scans. As discussed by B17, TAFTS utilises a thin film beam-splitter to cover the FIR spectral range. This is susceptible to vibration from the aircraft and can cause periodic miss-sampling of the interferogram which manifests as spectral ghosts in the raw spectra extending beyond the frequency band of the detectors. The laser sampling system and post processing corrects for the mis-sampling but some residual ghosting may still be present. Quality control procedures include checks for out-of-band signal above the noise level which if found result in the affected spectra being discarded. After quality control between two and six scans per cycle were deemed to be free of vibration effects.

3.2 The ARIES instrument

The ARIES instrument is a thermal infrared Fourier transform spectrometer capable of viewing both upwelling and downwelling radiance fields. Its spectral range is $550 – 3000$ cm^{-1} which is achieved utilising a sandwich detector comprised of MCT, covering $550 – 1600$ cm^{-1}, and InSb, covering $1400 – 3000$ cm^{-1}. The instrument has an unapodised spectral resolution of 1 cm^{-1}. The full field of view of ARIES is 2.5^{o} corresponding to an instantaneous footprint at the surface for this flight of approximately 260 m, with an acquisition time of 0.25 s per scan, smearing an individual scan by a further 35 m along track. To improve the signal-to-noise and better match the acquisition times of TAFTS nadir spectra we bin the ARIES observations into 5s intervals,

averaging the individual radiance scans made over this period so that the ARIES footprint over each 5 s average is 260 m x 960 m.

3.3 CIRCCREX/COSMICS Flight B898

In this study, we analyse FAAM Bae-146 flight B898 on the 19th March 2015. The flight path, shown in white in Figure 1, starts and ends at Keflavik International airport, Iceland. During the high level transit the Advanced Vertical Atmospheric Profiling System on the aircraft released 11 dropsondes, Vaisala RD94's, providing measurements of the atmospheric state below the aircraft. Additionally, in-situ measurements of true air temperature and water vapour mixing ratio were provided by a Rosemount de-iced temperature sensor and WVSS-II hygrometer fed from a modified Rosemount inlet (Vance *et al*., 2015), respectively. An on-board nadir viewing mini-lidar (Leosphere, ALS450) was used to identify the clear sky conditions analysed in this work (Wang et al., 2017) and also as a surface-to-aircraft range finder.

In this paper the observations considered are those made nearest in time and space to those exploited by B17, close to the summit of the Greenland Ice Sheet. Figure 1 indicates the location of the three closest TAFTS nadir cycles, from cycles 8-10. Crucially these also have coincident or near coincident ARIES upwelling radiance observations. Cycle 8 measurements were taken before the last dropsonde release while cycles 9 and 10 occurred afterwards. Following the completion of cycle 10 the aircraft descended to the surface, providing in-situ characterisation of the atmospheric profile. A summary of the cycle timings, location and along-track range in surface elevation is provided in Table 1. Table 1 also indicates the total column water vapour amount derived from the nearest dropsonde measurements.
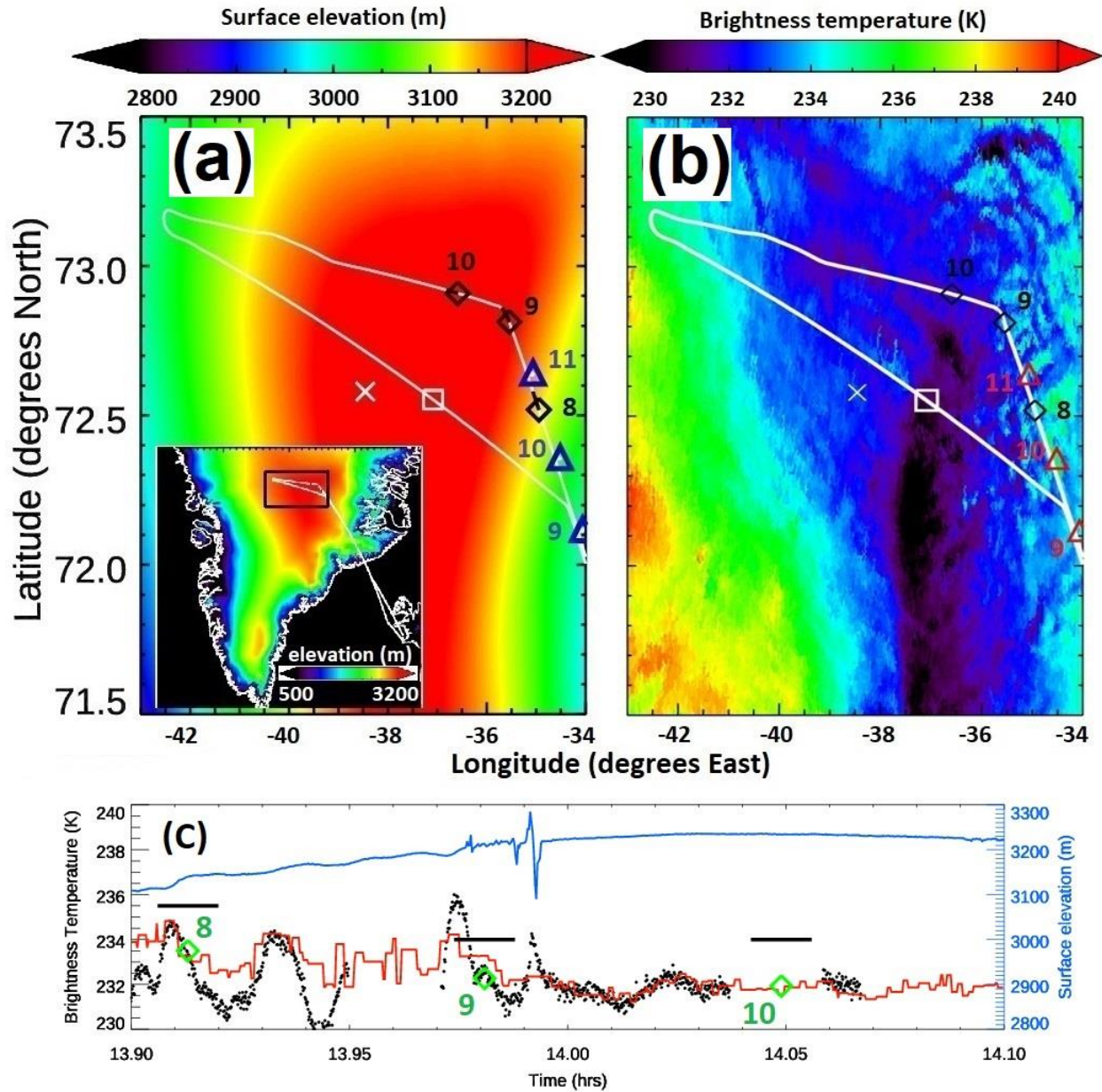
Figure 1. (a) Inset: B898 flight track and surface elevation over Greenland (surface elevation from GLOBE, 1999). Black box indicates the region highlighted in the main image; Main Image: Dropsonde release locations shown as blue triangles, the black diamonds represent the start of TAFTS nadir cycles with the black lines indicating the along track length of the nadir view. The white cross indicates the position of the Summit ground station and the white square the location of the low level emissivity measurements of B17. (b) Similar plot projected on the 13:20 UTC MODIS (Terra) 11 μm brightness temperature background. (c) The along flight track a-priori surface temperature (black stars) derived from ARIES assuming a surface emissivity of 0.995. In red are the spatially coincident MODIS (Terra) 11 μm brightness temperatures from 13:20 UTC. The green diamonds show the closest 12:00 UTC ERA interim surface temperature for cycles 8 to 10. The black horizontal bars above each cycle indicate the timing of the 50 second TAFTS nadir views. The blue line represents the surface elevation determined from the aircraft altitude and lidar return signal, the apparent rapid variation in surface elevation around 13.99 UTC is an artefact caused by the aircraft turn after cycle 9.

Nadir scan cycle	Data acquisition start time (UTC)	Mean surface elevation (m)	Elevation range(m)	Dropsonde total column water vapour (mm)	Cycle start location	Cycle end location
8	13.91	3142	18	0.42	72.52N 34.95W	72.58N 35.07W
9	13.97	3217	12	0.41	72.81N 35.54W	72.86N 35.70W
10	14.04	3245	0	0.40	72.91N 36.59W	72.92N 36.82W

Table 1. Timing and location details for each TAFTS nadir cycle. The mean and range in surface elevation during each cycle is determined from the lidar return signal. The total column water vapour for cycles 8, 9 and 10 is obtained from dropsonde 11 allowing for the variation in surface elevation between the cycles.

3.4 Simulation methodology

Equation 3 contains several terms that are not directly measured but can be inferred using a knowledge of the atmospheric profile in combination with radiative transfer modelling. The temperature and humidity profiles measured by dropsonde 11 are shown in Figure 2. To understand how variable the atmospheric temperature and humidity profiles are over a wider temporal and spatial scale, also shown is the profile from dropsonde 10 released 4 minutes earlier, nearest in time radiosonde ascents available from Summit station and the ERA5 (Copernicus Climate Change Service, 2017) total column water vapour for the same region as shown in figure 1. Figure 2 indicates relatively close agreement in both the temperature and humidity profiles above ~450 mbar as measured by all sonde sources. Between 450-600 mbar the humidity profiles for the dropsondes and sondes tend to diverge, with the 11:19 UTC Summit radiosonde release and the dropsondes notably drier than the later radiosonde measurements. Below 600 mbar the sonde-based humidity profiles all indicate the presence of a very dry layer. The ERA 5 plots (panels E-G) help understand the variations seen by the sondes. A very dry air mass is seen to be propagating from the SW towards the NE, coincidently sitting above Summit camp for the early sonde release and below the aircraft at the time of the high transit overpass.The variation in these profiles over the period highlights the importance of obtaining an independent characterisation of the atmospheric state which is as close as possible to the time and location of the radiance measurements.
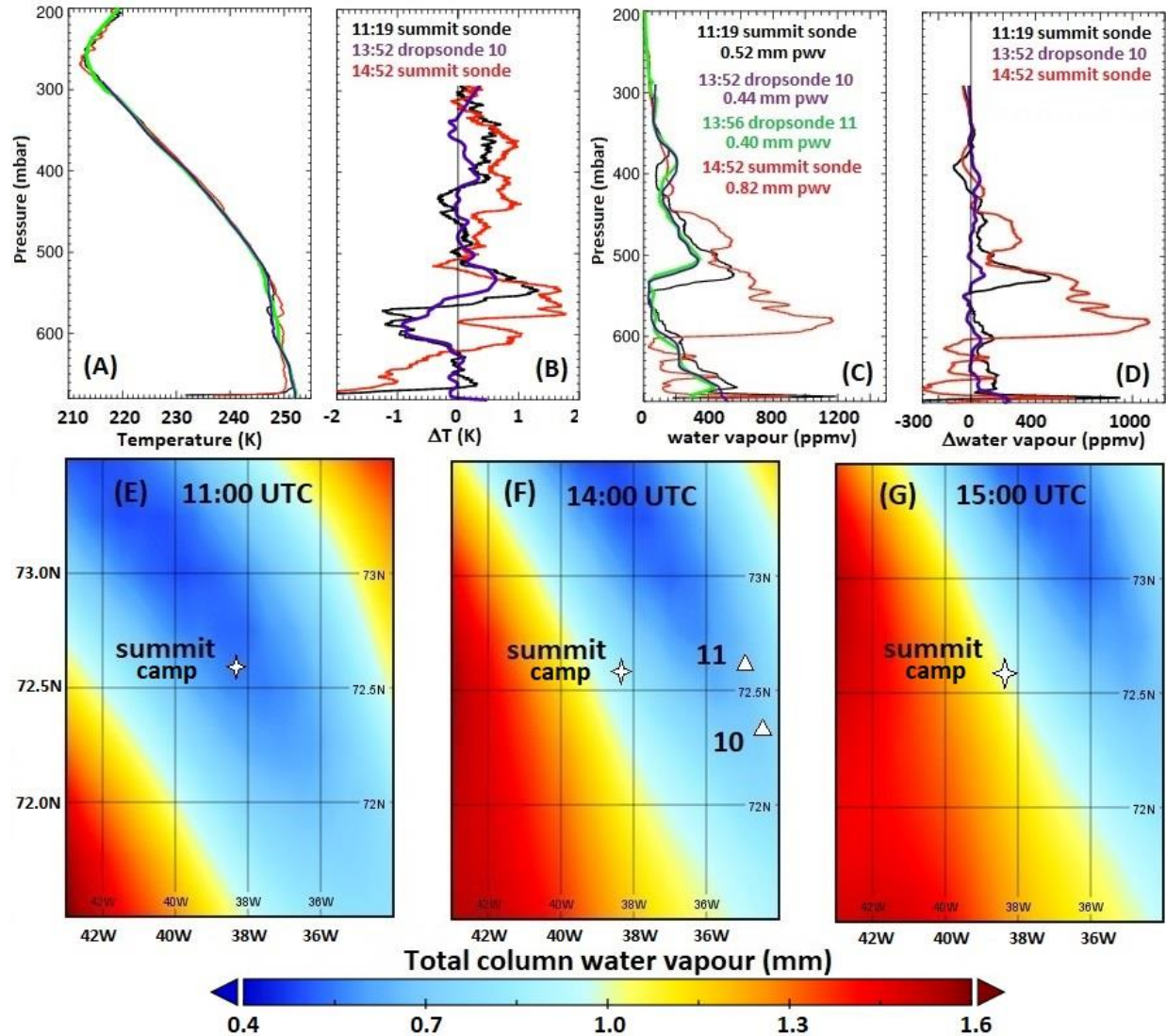
Figure 2. (A) Temperature profiles for dropsondes 10 (purple) and 11 (green) released from the aircraft at a pressure level of 287 mbar, and two sonde releases from Summit camp at 11:19 (black) and 14:52 UTC (red). (B) Temperature difference between dropsonde 10 and the two sondes and dropsonde 11. ERA-interim data is used to extend dropsonde 11 profiles to lower pressure levels. Panels (C and D) show the equivalent water vapour profiles and differences. Panels E – G show the ERA-5 total column water vapour at 11:00 UTC (E), 14:00 UTC (F) and 15:00 UTC (G), approximately corresponding to the release times of the various sondes.

As noted in the previous section, the emissivity retrievals performed here make use of the nearest dropsonde profile to the location of the TAFTS nadir cycles. Since the dropsondes do not start recording until about 300 m below the release height, the in-situ measurements of humidity and temperature from the aircraft at the time of release are used at the flight level. The atmospheric column above the aircraft is constructed from spatially coincident ERA-Interim (Dee *et al.*, 2011) data for the 19th March 2015 at 12:00 UTC. Ozone concentrations throughout the column are also taken from this ERA-Interim profile and the carbon dioxide concentration is set at 405 ppm, consistent with flask measurements from Summit (Dlugokencky et al., 2019). The resulting profiles and surface elevation data, determined from the aircraft lidar return signal, are used as

input to the radiative transfer code LBLRTM v12.7 (Clough et al., 2005) in order to calculate τ_ν, $L_{\nu,eff}^{\downarrow}$ and $L_\nu^{\uparrow}$.

3.5 Combining simulation and observed data sets

The simulations of transmission and radiance are performed at a resolution of at least 0.003 cm^{-1} in order to fully resolve features in the spectra. These simulated spectra are Fourier transformed to produce interferograms which then have the TAFTS and ARIES apodisation functions applied. To align wavelength scales and minimise effects due to differences in sampling between the simulation and measurements, all spectra are resampled onto the same frequency scale with a sampling of 0.01 cm^{-1}.

4. Results

4.1 Surface temperature retrievals

As discussed in section 2, we employ the technique used by Knuteson *et al* (2004) to derive a surface temperature prior to retrieving emissivity across the full spectral range. Figure 3 shows an example of a single ARIES up-welling spectrum from cycle 10 and the noise equivalent spectral radiance. Superposed on the spectrum is the atmospheric transmission, simulated using the associated dropsonde profile for the cycle, as well as surface emissivity estimates for snow and ice taken from the University of California Santa Barbara (UCSB) data base (Wan *et al*., 1994) which indicate a peak in emissivity at about 960 cm^{-1}. More recent ground-based in-situ measurements of MIR surface emissivity by Hori *et al*. (2006) also report that snow and ice show peak values of between 0.992-0.997 near 961 cm^{-1}. Figure 3 indicates that the atmosphere is highly transparent at this wavenumber, reaching values greater than 0.998. Based on these considerations, a-priori estimates of the surface temperature, T_{sap}, are determined for each 5 s average ARIES spectrum using the inverse Planck function:

$$T_{sap} = \int_{\nu_1}^{\nu_2} \frac{C_2\nu}{log\left(\frac{C_1\nu^3}{L_\nu/\varepsilon}+1\right)} \, \delta\nu \qquad (4)$$

where ν_1 = 960.5 cm^{-1} and ν_2 = 961.5 cm^{-1}, C_1 = 1.19104 x 10^{-8} W m^{-2} sr^{-1} (cm^{-1})$^{-4}$, C_2 = 1.43877 K (cm^{-1})$^{-1}$ and L_ν is the averaged spectral radiance. We assume a surface emissivity, ε, of 0.995 over the integration range. Note that this step is performed purely to reduce the number of iterations required in the surface temperature retrieval process.
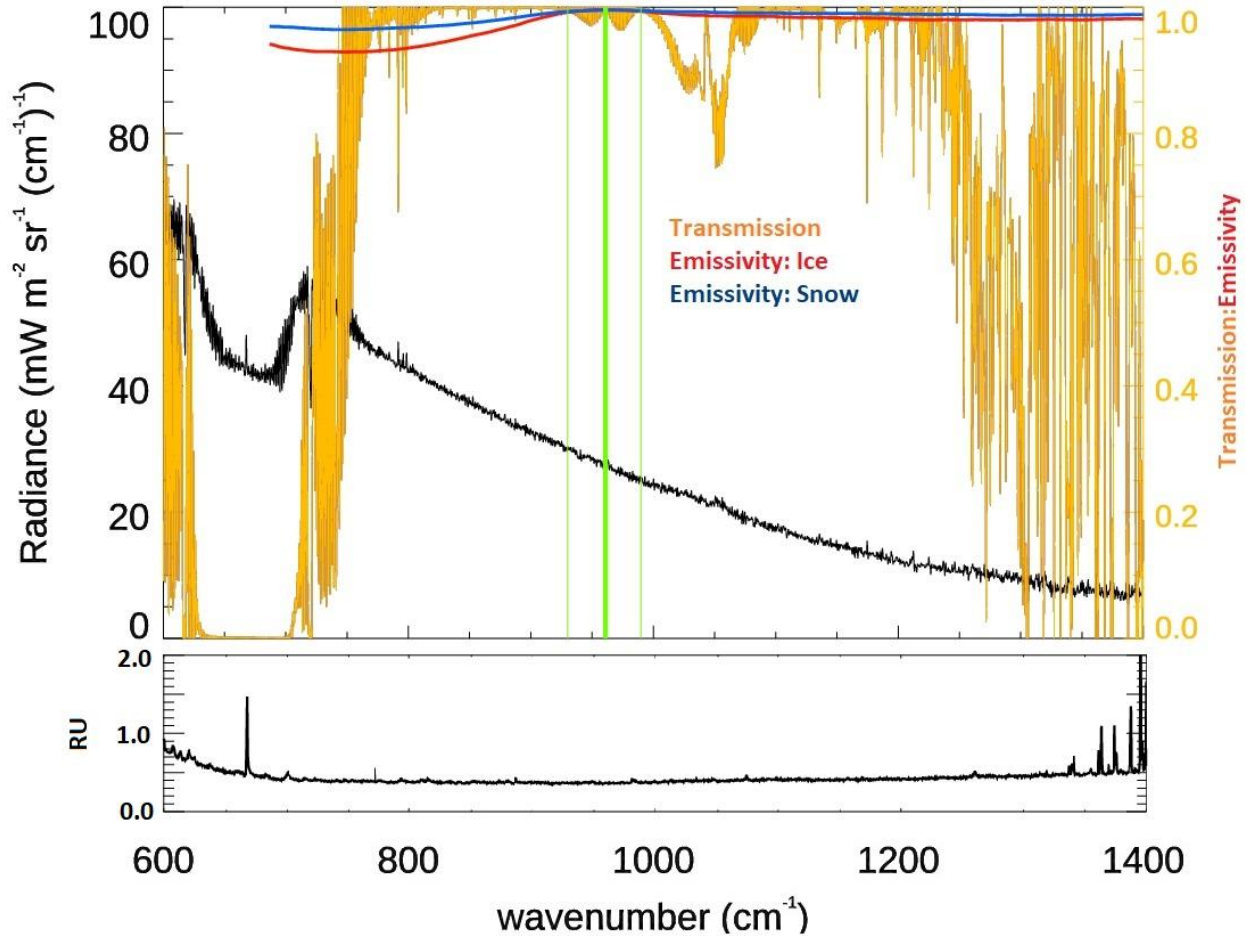
Figure 3. Upper panel: Typical ARIES nadir observation from cycle 10. Over-plotted in orange is the atmospheric transmission derived from LBLRTM using the relevant dropsonde interpolated atmospheric profile. The red and blue curves show ice and snow emissivity, respectively, as given by UCSB, Mammoth Lakes SNOW_1 and ICE01 (Wan *et al*., 1994). The central thick green line indicates the wavenumber band used to derive the a-priori surface temperature estimate and the light green lines to either side indicate the regions covered by the CO_2 P and R branches used in the surface temperature retrieval. Lower panel: The ARIES noise equivalent spectral radiance, 1 RU= 1mW m^{-2} sr^{-1} (cm^{-1})$^{-1}$.

There are up to 10 ARIES average radiance spectra for each TAFTS nadir cycle. For each average spectrum, spectral emissivities over the 930-960 and 960-990 cm^{-1}, P and R branches are retrieved using equation 2, as a function of surface temperature. We vary T_s in steps of 0.1 K over a 4 K range centred on T_{sap} noting the standard deviation in the emissivity across each band for every 0.1 K increment. The retrieved surface temperatures, T_{sp} and T_{sr}, are the values which minimise the standard deviation in the P and R branches respectively.

Figure 4(a-c) shows plots of these standard deviations across each band as a function of surface temperature for the first three ARIES average spectra from cycle 9. The plots clearly show that the variance in emissivity over the R-branch has a greater sensitivity to surface temperature changes. This is typical for all the ARIES average spectra and may be attributable to the stronger absorption lines in this branch of the CO_2 lasing lines. For each ARIES average we define the retrieved surface temperature as simply:

$$T_S = \frac{(Tsp + Tsr)}{2} \tag{5}$$

Since the retrieved surface temperature should not vary with wavenumber the difference between T_{sp} and T_{sr} provides a first order estimate of the uncertainty associated with a given T_s. Figure 4(d) shows these differences between the retrieved surface temperatures for the P and R branches for the twenty-two ARIES averages spanning cycles 8-10. An additional source of systematic uncertainty is introduced by the ARIES calibration stability over the three cycles, ΔT_{cal}, which is estimated at 0.2 K (S. Fox, personal communication, 2020). Instrument noise ΔT_{ins} on the averaged spectra is about 0.06 mW m^{-2} sr^{-1} (cm^{-1})$^{-1}$ this value can be compared to the minima in the emissivity standard deviation, figure 4(a-c), these minima are about 0.003 which equates to 0.1 K or 0.08 mW m^{-2} sr^{-1} (cm^{-1})$^{-1}$ at a surface temperature of 232 K suggesting, as expected, that the minimisation is limited by instrument noise. The overall uncertainty for the surface temperature is then given as

$$\Delta T_s = \sqrt{[\Delta T'^2_S + \Delta T^2_{cal} + \Delta T^2_{ins}]} \tag{6}$$

where $\Delta T'_s$ is the standard deviation in the differences shown in Figure 4(d) and is equal to 0.45 K. Applying (6) results in an estimated overall uncertainty of 0.5 K on the retrieved surface temperatures. Figure 4(e) shows these retrieved surface temperatures for each TAFTS nadir cycle relative to the start time of each scan cycle.
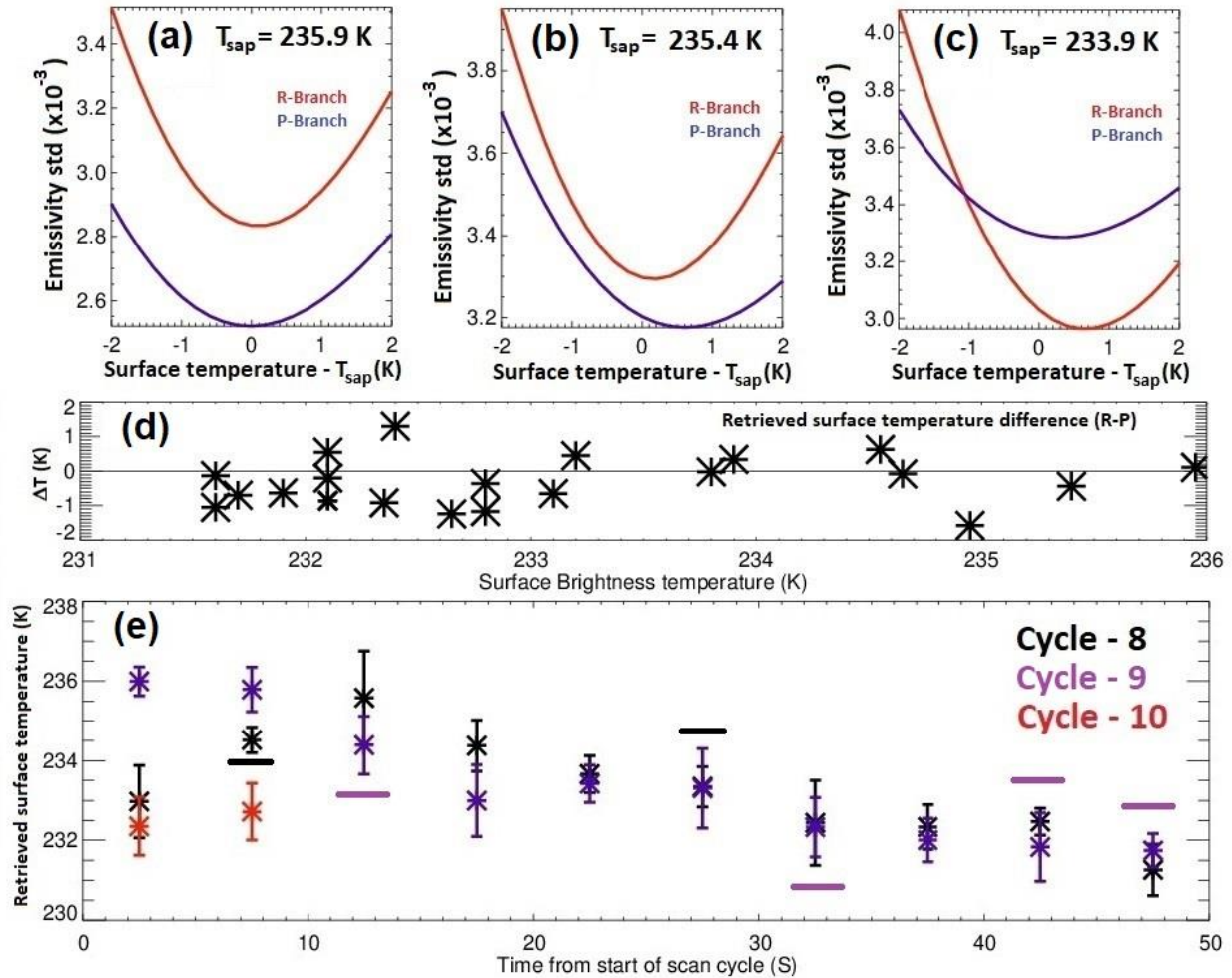
Figure 4. Panels a-c: Examples of the standard deviation in retrieved emissivity over the P and R branch (see text for details). Panel d shows the difference in the surface temperature retrievals between the two branches plotted against the a-priori surface brightness temperature. Panel e: Retrieved surface temperature for each ARIES average spectrum relative to the start of individual scan cycles (Cycle 10 ARIES scans are off-set in time by 10 s as these data were acquired just prior to TAFTS data). The horizontal bars indicate the ARIES spectra that have coincident TAFTS measurements, colour coded according to cycle.

While cycles 8 and 9 have coincident TAFTS and ARIES measurements, for cycle 10 the ARIES nadir observations finish just before the TAFTS scans commence (Figure 1c). In order to be consistent with the methodology for surface temperature retrieval applied to cycles 8 and 9 we use the ARIES surface temperature retrievals made just prior to cycle 10 to perform the emissivity retrievals from the cycle 10 TAFTS measurements. Figure 1c provides a justification for this approach. First, the figure indicates remarkable consistency between the ARIES a-priori surface temperature estimates and the 11 μm MODIS brightness temperatures recorded along the flight track 40-46 minutes earlier. Second, the along track variance in the 11 μm MODIS brightness temperature for locations sampled just before and during TAFTS cycle 10 is small, with a standard deviation of 0.3 K. Taken together, these findings imply that the surface temperature estimates from ARIES just prior to cycle 10 will be representative of the values encountered during the cycle.

Finally, we note that the use of the P and R branch means that the surface temperature retrieval is dependent on the CO_2 column used in the radiative transfer simulation. Surface flask measurements have an accuracy of 0.1 ppm or better but the vertical gradient in CO_2 concentration can be significant between the boundary layer and free troposphere (e.g. Sweeney et al., 2015). Aircraft observations over the Arctic (Conway and Steele, 1989) suggest 5 ppm is a reasonable upper estimate of vertical variability and so we re-run the retrieval using a column concentration of 410 ppm. Comparing the results to the 'control', 405 ppm case we find a reduction in the retrieved surface temperature of about 0.05K.

4.2 Surface emissivity retrievals

Substituting the simulated values of τ_ν, $L_{\nu,eff}^\downarrow$ and $L_\nu^\uparrow$, the appropriate estimate of T_s, and both the TAFTS and ARIES upwelling radiance measurements into Equation (2) allows the retrieval of surface emissivity at infrared wavelengths sensitive to surface emission. In the FIR, strong water vapour absorption can significantly reduce the surface to aircraft transmission such that surface emissivity can only be retrieved with confidence in isolated micro-window regions of varying spectral width. In contrast, excepting the 1042 cm^{-1} ozone band, across the main atmospheric window region in the MIR (750-1200 cm^{-1}) the atmospheric transmission is high (Figure 3), allowing retrievals to be performed over a much wider, continuous spectral range. Because of these considerations, the implementation of the emissivity retrieval in the two spectral regions covered by ARIES and TAFTS is subtly different and is considered separately for each regime in sections 4.2.2 and 4.2.3. The main sources of uncertainty in both regimes are however similar, and those related to the simulation of atmospheric transmittances and radiances are discussed and quantified in the next section.

4.2.1 Sources of uncertainty on retrieved emissivity

Uncertainty in the emissivity retrieval arises from a number of sources including instrument noise and calibration, and the quality of the surface temperature retrievals previously discussed. The emissivity retrieval is also impacted by imperfect knowledge of (a) the atmospheric state below the aircraft, (b) the underlying spectroscopy of the principal gaseous absorbers and (c) the path length from the surface to the aircraft. To assess the impact of (a)-(c) we perturb each contributing factor in turn, holding the remainder fixed at their control values (section 3.4) and compare the resulting emissivities to those obtained using the control set-up.

The atmospheric state impacts the emissivity retrievals through its effect on the simulated transmission and atmospheric radiance in equation 2. Major contributions to the emissivity error budget come from the uncertainties in the atmospheric temperature and humidity profile. We estimate the uncertainty in atmospheric temperature to be 0.2 K (Vomel *et al.* 2016) which we treat as systematic offset throughout the column. For humidity we refer to Miloshevich *et al.* (2009) and assume the uncertainty has two components arising from sensor calibration and 'production variability'. The impact of sensor calibration is estimated to be ±5 % of the measured relative humidity value plus an absolute offset of ± 0.5 %. 'Production variability' is estimated to be ±1.5% of relative humidity values above 10 % or ±3% for values below 10%. Combining these uncertainties in a 'worst-case' scenario we increase the water vapour column by 7% where the column relative humidity is above 10% and by 8.5% where the column relative humidity is below 10%, which occurs between 530 and 600 mb.

We evaluate the effect of uncertainties in water vapour spectroscopy by perturbing the foreign component of the continuum by 14 % and 7 % in two separate runs, following Mlawer et al.

(2019). While there is little information on the uncertainty in the self-broadened component of the continuum, we perform an additional run, perturbing its strength by 10 %. Finally, the uncertainty in geometrical path length is linked to our knowledge of the surface elevation, which we perturb by 10 m.

Figure 5 shows the impact of these perturbations on the retrieved emissivity for an example case from cycle 8. Other cases show similar behaviour. The MIR shows little sensitivity, with the largest effect, albeit still below 0.0005, seen in the ozone absorption band in response to the perturbation in atmospheric temperature. The impact of the perturbations is typically an order of magnitude larger in the FIR, a reflection of the greater atmospheric opacity in this region. The largest impacts are due to uncertainties in the water vapour column and the foreign broadened component of the water vapour continuum and reach up to 0.005. Below 400 cm^{-1} the effects of perturbations to both the temperature profile and surface elevation start to become noticeable, reaching 0.001.

In addition to the somewhat idealized perturbations applied above, we also attempt to gain an understanding of the alongtrack variation of the atmosphere indicated in figure 2 by replacing the profiles from dropsonde 11 with that from dropsonde 10. The profile shapes are very similar for the two (Figure 2(A, C)) but a small absolute increase in the near surface concentration of water vapour indicated by dropsonde 10 (Figure 2(D)) results in an overall 10 % increase in the total column water vapour. The resultant change in the retrieved emissivity is consistent with the changes obtained when applying generic adjustments of 7 – 8.5% to account for the dropsonde humidity uncertainty. It should be noted that linearly interpolating between the dropsonde 10 and 11 profiles to the position of cycle 8 (Figure 1) would actually result in a 4 % change to the total column water vapour compared to that measured by dropsonde 11, well within the the 7-8.5 % uncertainty estimated for the dropsonde humidity measurements.
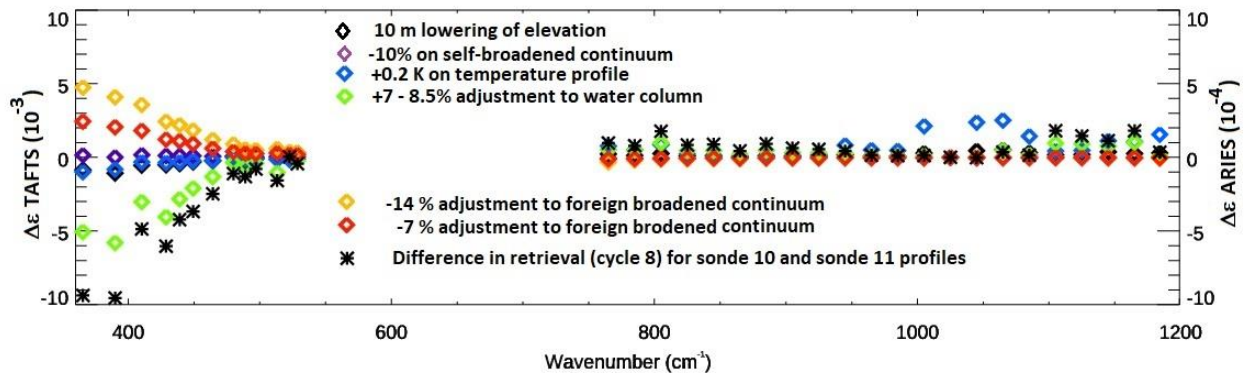

Figure 5: Impact of uncertainties in retrieved emissivity due to changes in atmospheric state, path length and spectroscopy for cycle 8, expressed as the difference in retrieved emissivity, Δε, between the perturbed and the control case. Note that Δε over the TAFTS range is an order of magnitude larger than over the ARIES range.

4.2.2 MIR emissivity retrievals from ARIES

We use the retrieved surface temperatures with their corresponding 5 s average ARIES radiances to retrieve spectral emissivity estimates at the instrument resolution of 1 cm^{-1}. These spectral emissivities are then averaged over 10 cm^{-1} bands at 20 cm^{-1} intervals, with the caveat that the atmospheric transmission has to exceed 0.95 for a retrieval to be included in the average. We

focus on those cases that have co-located or near co-located TAFTS observations. As shown in figure 4(e) and discussed previously, for cycle 8 we have two coincident sets of TAFTS and ARIES spectra, for cycle 9 there are four, and for cycle 10 we use the two ARIES average spectra from just prior to the cycle. The resulting eight sets of retrieved MIR emissivities are shown in Figure 6 (panels a-h).

The uncertainty in the retrieved emissivities due to ΔT_s is shown by the blue vertical bars plotted to the right of each emissivity value. These uncertainties are spectrally coherent and represent the range over which the retrieved spectral emissivity may be shifted in response to a change in surface temperature of ΔT_s. Comparing Figure 6 to 5 it is obvious that the uncertainty in surface temperature dominates the error budget across this wavenumber range. For completeness, the standard deviation of the averaged retrieved emissivity within each 10 cm^{-1} interval is shown by the black vertical bars.

While it is not easy to discern marked changes between the emissivities retrieved from the different cycles there is a general tendency for values to reduce from an average baseline of ~0.99 to ~0.98 as the aircraft ascends towards the summit of the plateau (compare Panels g and h to a and b). This reduction also means that the retrieved values from both spectra in cycle 10 can be robustly classified as different from 1.0. The shape of any given spectrum is relatively flat, although the final two spectra in cycle 9 and both spectra in cycle 10 do show coherent features, with minima at 780 and 1040 cm^{-1} and maximum values between 1100-1200 cm^{-1}. It is also worth noting that the slightly reduced atmospheric transmission at wavenumbers greater than 1000 cm^{-1} compared to lower frequencies (see Figure 3) translates to a larger standard deviation in the retrieved emissivity in any given 10 cm^{-1} band. Similar spectral behaviour is seen in terms of the effects of the uncertainty in T_s.

Panels g and h also show the MIR retrievals made from the low-level flight described in B17. The wavenumber bands chosen for these earlier retrievals were selected based on a desire to make comparisons with an existing theoretical model of snow and ice emissivity (Chen et al., 2014) and may not be the optimal choice, particularly in the FIR (see next section). Figure 1 also shows that the location of the low-level measurements was some distance from those taken during cycle 10. Given this, the level of agreement between the retrievals, both in terms of absolute level and spectral shape is encouraging.
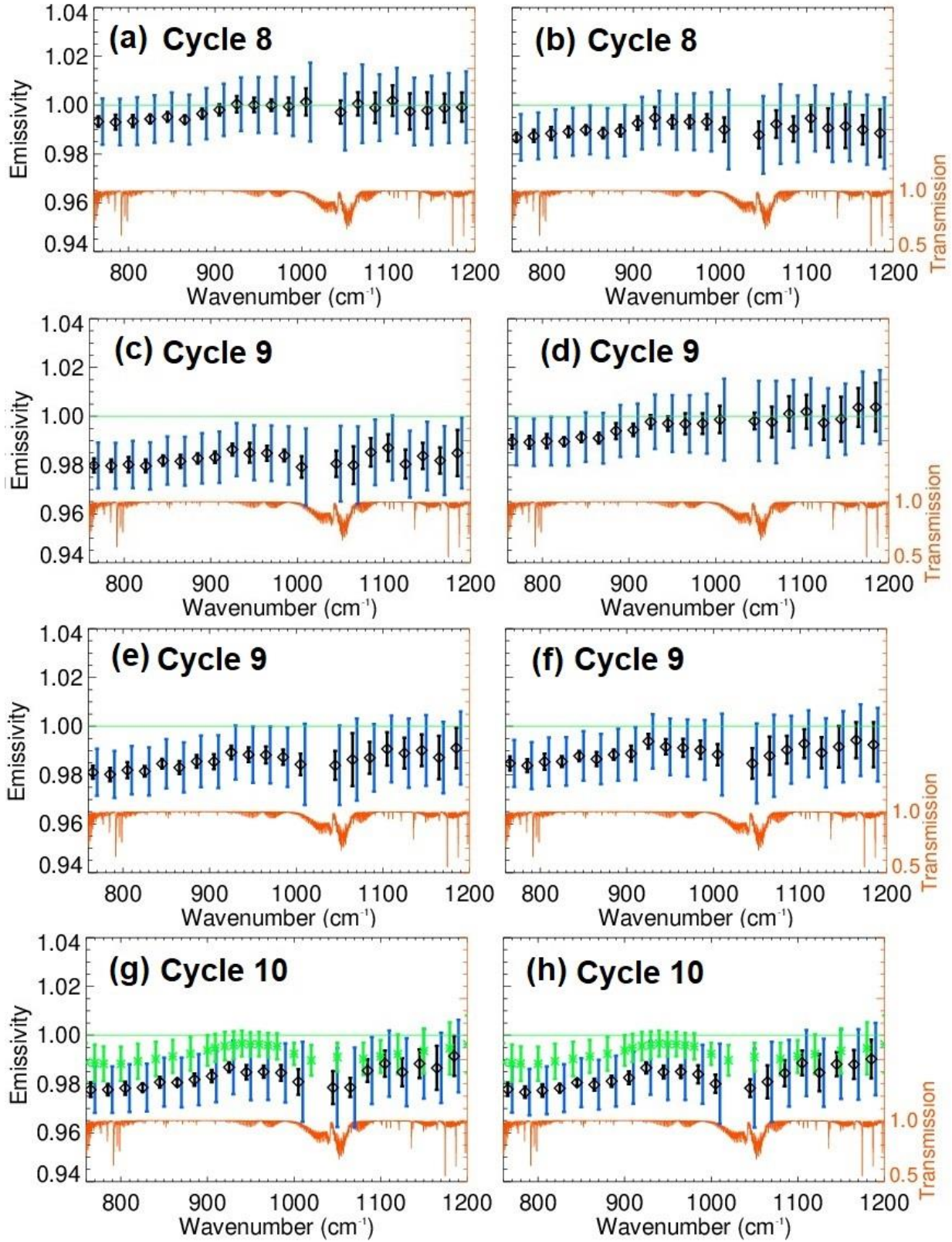
Figure 6: MIR surface emissivities retrieved from the 5 s average ARIES radiance spectra colocated with TAFTS spectra. Panels a and b correspond to cycle 8, Panels c-f to cycle 9 and g and h to cycle 10. Uncertainties resulting

from the surface temperature retrievals are shown in blue. The black bars indicate the standard deviation in the retreived emissivity within each 10 cm^{-1} band. The emissivities derived by B17 are shown in green in panels g and h. Orange lines show the simulated transmission of the layer between the surface and the FAAM aircraft.

4.2.3 FIR emissivity retrievals from TAFTS

For TAFTS, there are fewer spectra per cycle than observed by ARIES, due to the lower scan repetition of the TAFTS instrument, and the quality control which excluded about 75 % of spectra. Figure 7 shows examples of upwelling FIR radiance spectra taken during cycles 8 to 10, the simulated atmospheric transmission for cycle 10 and the single scan NESR.
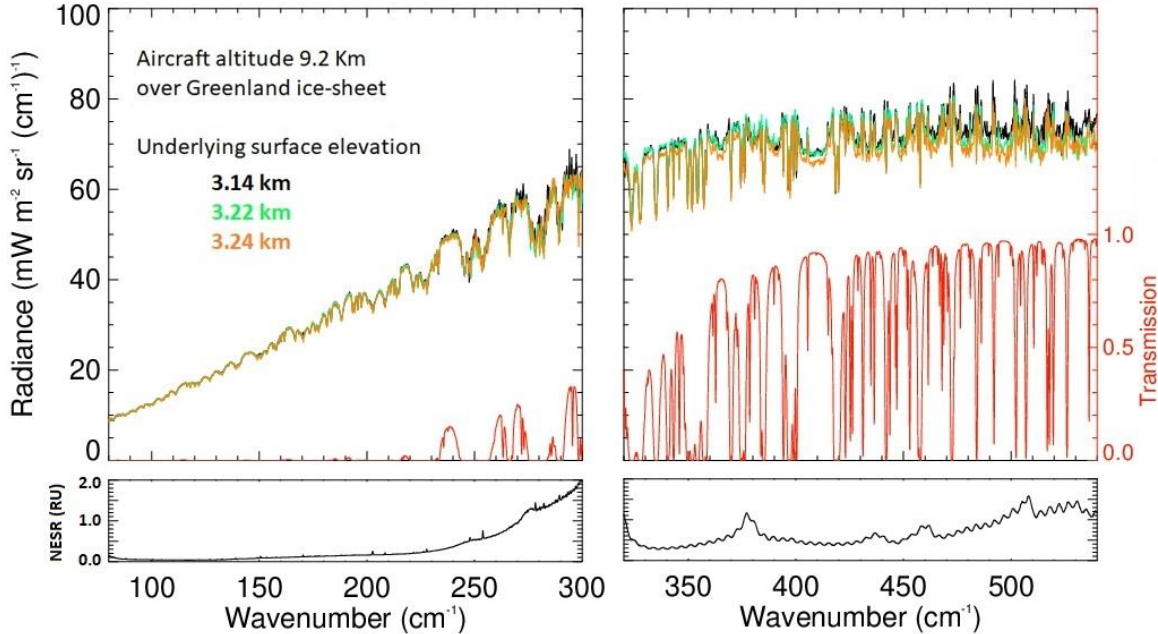
Figure 7. TAFTS nadir radiances for selected scans and cycles. The panel on the left are radiances acquired from TAFTS longwave channel and the panel on the right from TAFTS shortwave channel. Shown in red is the associated atmospheric transmission, derived from LBLRTM, for cycle 10. Lower panels show the noise equivalent spectral radiance, 1 RU = 1mW m^{-2} sr^{-1} (cm^{-1})$^{-1}$.

Following B17, emissivities in the FIR are retrieved at a resolution of 0.25 cm^{-1} and only where the simulated atmospheric transmission between the surface and aircraft exceeds a certain threshold. In B17 this threshold was set at 95% for the TAFTS shortwave channel. For the measurements described here the increased path length means that the atmospheric opacity is considerably higher. To account for this we have set the transmission threshold at 60% over selected micro-windows in order to retrieve emissivity over a similar spectral range to B17, excluding the sharp absorption features associated with water vapour that are apparent in some of the windows. The emissivity retrievals within each selected micro-window, shown in figure 8 by the horizontal blue bars, are then averaged to give the emissivity values shown in the figure. As for Figure 6, the blue vertical bars indicate the range in retrieved emissivity that arises given the uncertainty in the retrieved surface temperatures from ARIES. The black vertical bars show the combination of the uncertainty in TAFTS calibration, approximately 0.3 K, instrument noise and the standard deviation of averaged emissivity within each micro-window.

Figure 8 indicates that the spectral shape of the retrievals is relatively consistent within cycle 8 (a,b) and within cycle 10 (g, h) although there are obvious differences between the two cycles. More 'within cycle' variation is seen during cycle 9 (c-f). Nonetheless, in the majority of cases the emissivity tends to be a minimum at ~410 cm^{-1}. This minimum deepens as the aircraft progresses towards the summit of the plateau (panels g and h), reaching values as low as 0.9. Exceptions to this minimum position occur in cycle 9 (panels d-f) where it is shifted to larger wavenumbers and there is some hint of a bi-modal shape. Similar to the MIR results, comparisons with the retrievals from B17 over this spectral range (panels g and h) show very good agreement at wavenumbers > 390 cm^{-1}, notwithstanding the different bands over which emissivities were averaged. The larger error bars in B17 are likely due to a number of factors including this difference in band selection combined with the use of a profile that was not so closely co-located with the aircraft observations, and the incorporation of TAFTS zenith and nadir aircraft measurements in the retrieval process, amplifying the influence of measurement uncertainty.
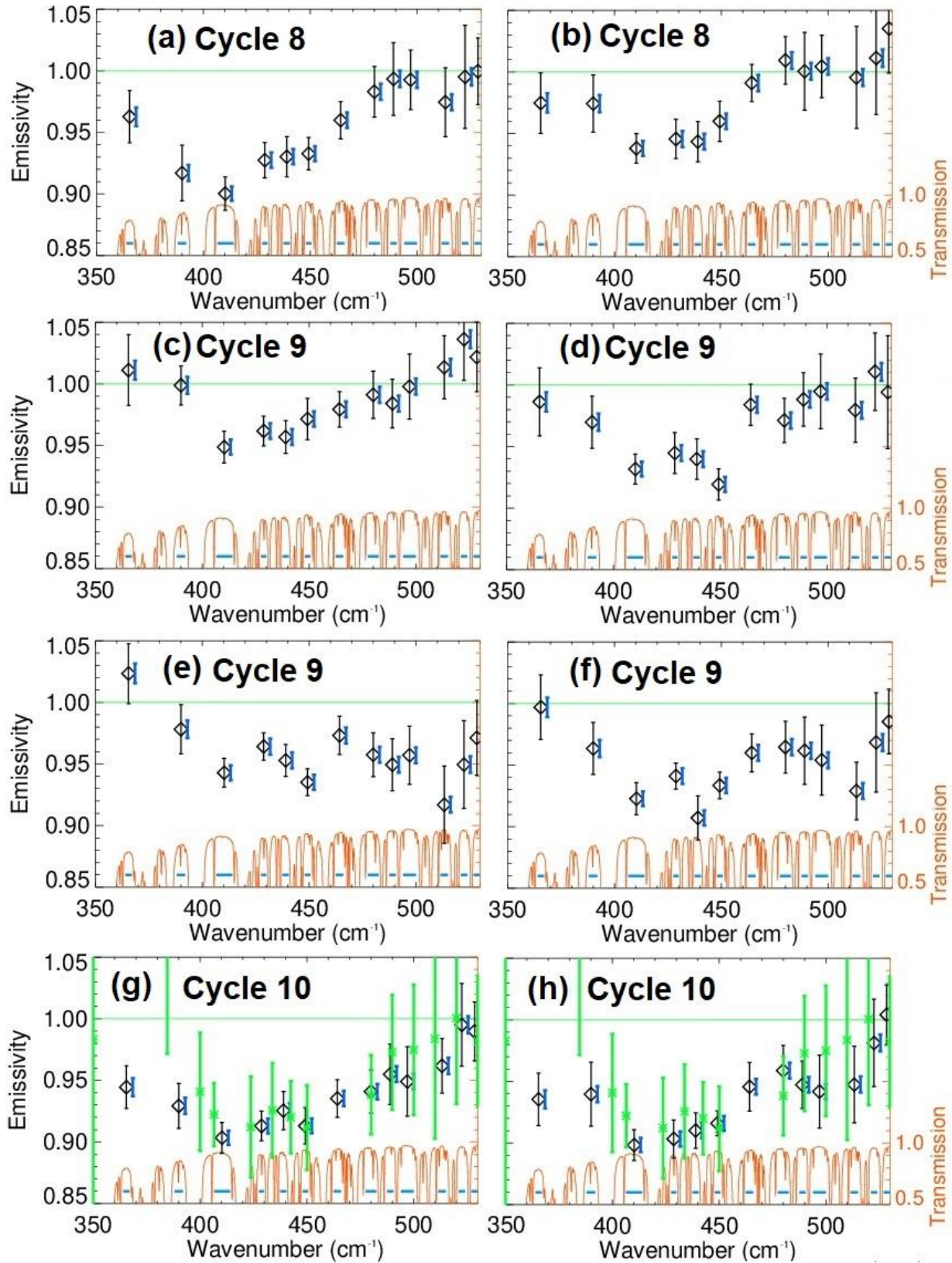
Figure 8: Retrieved FIR emissivity from TAFTS for cycles 8-10. The emissivity is averaged over discrete wavenumber bands coincident with regions of high transmission, shown in blue. The black error bars indicate the uncertainty associated with TAFTS calibration, instrument noise and the variation in the emissivity retrievals within each micro-window. The vertical blue bars to the right indicts the uncertainty in the retrieved emissivity associated with ΔT_s. Plotted in green, in panels g and h, are the retrieved emissivities and their corresponding uncertainties from B17.

5. Discussion and Conclusions

The aim of this study was to investigate the feasibility of retrieving far infrared surface emissivity from remotely sensed nadir radiance observations made from an aircraft flight over the Greenland Plateau. While Bellisario *et al*. (2017) successfully used near surface observations from the same flight to obtain surface emissivity estimates across the infrared, to the best of our knowledge, this is the first time a similar endeavour has been attempted using interferometer observations made from high altitude. The challenges encountered here are more representative of those faced by future satellite missions operating in the far infrared that have, as one of their goals, the characterisation of high latitude surface emissivity, such as NASA's Polar Radiant Energy in the Far Infra Red Experiment (PREFIRE) and Far-infrared Outgoing Radiation Understanding and Monitoring (FORUM), ESA's 9th Earth Explorer.

Our retrieval approach has two steps: first estimates of surface temperature are obtained from mid-infrared radiances in two narrow bands following the approach of Knuteson *et al*. (2004). These estimates are then used to infer surface emissivity across the infrared using the observations from TAFTS (FIR) and ARIES (MIR) in combination with high resolution radiative transfer modelling. Retrievals are performed for three sets of measurements made as the aircraft flew towards the interior of the Plateau, sampling successively higher surface elevations.

Retrievals of emissivities from the closest cycle of measurements to the low level observations analysed in Bellisario et al. (2017) agree within the uncertainties associated with both sets of retrievals, suggesting that the approach used here is, to first order successfully accounting for the longer atmospheric path for these high altitude retrievals and the 1.5 K difference in the underlying surface temperature. We note that this comparison of emissivity between B17 and cycle 10 are for underlying surfaces that are temporally and spatially offset. However, since we are near the highest elevation of the ice sheet for both B17 and cycle 10 it seems reasonable to assume that any variation in emissivity will be small compared to varibility in surface temperature and the overlying atmospheric column (see Figure 2) and that these factors would be expected to have the dominant effect on the infrared radiance signal (see Figure 5).
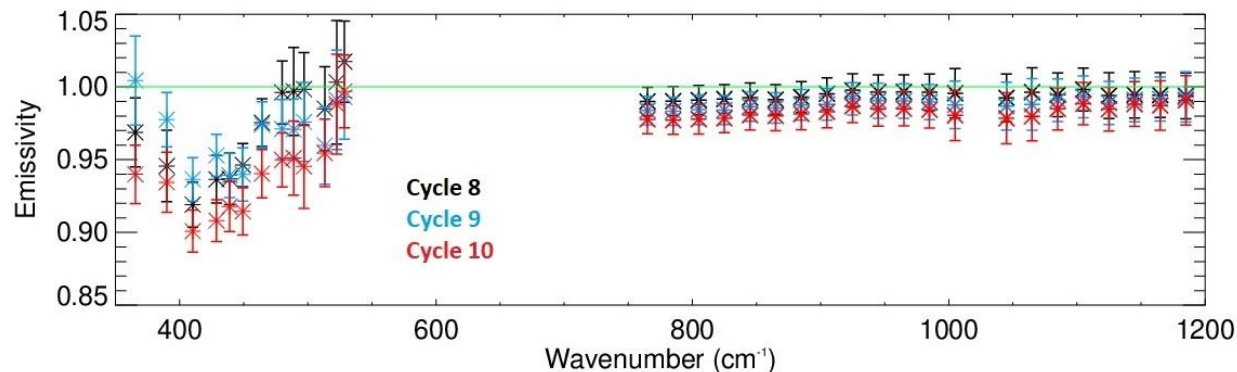
Figure 9. Averaged emissivity covering both the TAFTS and ARIES spectral range for each of the 3 cycles

More generally, in the MIR there is a tendency for emissivities to reduce from an average baseline of ~0.99 to ~0.98 as the aircraft ascends towards the summit of the plateau (Figure 9). In this spectral region the retrieved emissivities are relatively flat, although the four spectra, Figure 6 (panels E-G), nearest the summit do show coherent features, with minima at 780 and 1040 cm^{-1} and maximum values between 1100-1200 cm^{-1}. In the FIR there is a much more pronounced spectral variation in emissivity in our selected micro-windows, within the "dirty window" region of the FIR, around 20 μm (Rathke, 2002). Indeed, consideration of results from all the retrievals suggests that the surface emissivity is significantly less than unity in the 'dirty window' region that lies between 380-450 cm^{-1}, reaching values as low as 0.9.

Our results indicate that the dominant source of uncertainty in our emissivity retrievals within the MIR arises from the uncertainty associated with the surface temperature retrieval. The approach used here yields typical surface temperature uncertainties of 0.5 K which equate to emissivity uncertainties of 0.01 for wavenumbers between 400-550 cm^{-1} and 800-1000 cm^{-1}, and slightly higher values of up to 0.015 between 1070-1200 cm^{-1}. In the FIR the TAFTS measurement uncertainty is the dominant error source. Instrument noise translates to emissivity uncertainties ranging from 0.01 in the centre of the TAFTS shortwave channel (~ 460 cm^{-1}) to values of up to 0.03 towards the shortwave detector band edge (~ 530 cm^{-1}). Other potential sources of uncertainty, such as knowledge of the atmospheric profile and underlying water vapour spectroscopy play a second order or negligible role for the dry, cold conditions sampled here, although extending the retrievals to lower wavenumbers would amplify the effects of these uncertainties. In addition, a higher water column , such as that observed above Summit camp at 14:52 UTC, will reduce the number and spectral widths of the micro-windows that can be used for FIR surface emissivity retrieval from space.

In summary, the results presented in this study provide further evidence that snow and ice surface emissivity in the far-infrared is substantially less than unity and has a distinct spectral shape. They highlight that, as expected, the uncertainty in the emissivity retrieval is strongly tied to the confidence with which the surface temperature can be derived. However, in the far-infrared, TAFTS instrument noise is equally important in driving the uncertainty budget. This noise is primarily related to the vibration environment of the FAAM aircraft, an issue which also limits the number of spectra available for analysis. Such platform environment issues should be mitigated for a satellite instrument although it is worth noting that the noise target for the

FORUM Sounding Instrument is 0.4 mW m^{-2} sr^{-1} (cm^{-1})$^{-1}$ across the far-infrared, which is similar to that of the TAFTS shortwave channel in the range 320 cm^{-1} to 450 cm^{-1} (Figure 7).

The results also show that it is feasible to retrieve far-infrared surface emissivity from spectrally resolved radiances measured at altitude. However, the particular measurements exploited here were made on an opportunistic basis as part of a wider campaign which was not focused on emissivity retrieval. To make further progress in (a) evaluating existing theoretical emissivity models such as that developed by Chen et al. (2014) and (b) assessing the likely retrieval performance of the PREFIRE and FORUM instruments we strongly advocate targeted flights over sites with equivalent ground-based radiometric instrumentation, independent surface skin temperature monitoring capability, and where the snow and ice conditions can also be assessed in-situ. Clearly for objective (b) the impact of the specific instrument configurations should also be investigated along with the possible degradation in retrieval performance due to sub-scene inhomogeneity and/or the absence of a co-located estimate of the underlying atmospheric state. As part of these investigations the use of a multi-target retrieval approach from the radiance measurements themselves would also be worth exploring.

Acknowledgments, Samples, and Data

References

Andre, C., C. Ottle, A. Royer and F. Maignan (2015). Land surface temperature retrieval over circumpolar Arctic using SSM/I-SSMIS and MODIS data, Rem. Sens. Env., 162, 1-10

Bantges, R., H. Brindley, J. Murray, A. Last, C. Fox, S. Fox, C. Harlow, S. O'Shea, K. Bower, B. Baum, P. Yang and J. Pickering, (2020), A test of the ability of current bulk optical models to

represent the radiative properties of cirrus cloud across the mid- and far-infrared, Atmos. Chem. Phys. Disc., doi:10.5194/acp-2019-1181

Bellisario, C., H. Brindley, J. Murray, A. Last, J. Pickering, C. Harlow, S. Fox, C. Fox, S. Newman, M. Smith, D. Anderson, X. Huang and X. Chen, (2017), Retrievals of the far infrared surface emissivity over the Greenland Plateau using the Tropospheric Airborne Fourier Transform Spectrometer (TAFTS), J. Geophys. Res., 122, 12,152-12,166, doi: 10.1002/2017JD027328

Blanchard, Y., J. Pelon, E. Eloranta, K. Moran, J. Delanoe and G. Seze, (2014), A synergistic analysis of cloud cover and vertical distribution from the A-train and ground-based sensors over the high Arctic station Eureka from 2006-2010, J. Appl. Met. Clim., 53, 2553-2570

Canas, T. A., Murray, J. E., and Harries, J. E. (1997). Tropospheric Airborne Fourier Transform Spectrometer (TAFTS). Satellite Remote Sensing of Clouds and the Atmosphere II, 3220, 91–102. Proceedings Volume 3220, Satellite Remote Sensing of Clouds and the Atmosphere II; https://doi.org/10.1117/12.301139

Chen, X., Huang, X., & Flanner, M. G. (2014). Sensitivity of modeled far-IR radiation budgets in polar continents to treatments of snow surface and ice cloud radiative properties. Geophysical Research Letters, 41, 6530–6537. https://doi.org/10.1002/2014GL061216

Clough, S., Shephard, M., Mlawer, E., Delamere, J., Iacono, M., Cady-Pereira, K.,…Brown, P. (2005). Atmospheric radiative transfer modeling: A summary of the AER codes. Journal of Quantitative Spectroscopy and Radiative Transfer, 91(2), 233–244. https://doi.org/10.1016/j.jqsrt.2004.05.058

T. Conway and L. Steele, (1989) Carbon dioxide and methane in the Arctic atmosphere, J. Atmos. Chem., 9, 81-99

Copernicus Climate Change Service (C3S) (2017): ERA5: Fifth generation of ECMWF atmospheric reanalyses of the global climate . Copernicus Climate Change Service Climate Data Store (CDS), *date of access*. https://cds.climate.copernicus.eu/cdsapp#!/home

Cox, C., J. Harries, J. Taylor, P. Green, A. Baran, J. Pickering, A. Last and J. Murray, (2010), Measurements and simulation of mid and far infrared spectra in the presence of cirrus, Q. J. Roy. Meteorol. Soc., 136, 718-739

Dee, D. P., Uppala, S. M., Simmons, A. J., Berrisford, P., Poli, P., Kobayashi, S.,…Vitart, F. (2011). The ERA-Interim reanalysis: Configuration and performance of the data assimilation system. Quarterly Journal of the Royal Meteorological Society, 137(656), 553–597. https://doi.org/10.1002/qj.828

Dlugokencky, E.J., J.W. Mund, A.M. Crotwell, M.J. Crotwell, and K.W. Thoning (2019), Atmospheric Carbon Dioxide Dry Air Mole Fractions from the NOAA ESRL Carbon Cycle Cooperative Global Air Sampling Network, 1968-2018, Version: 2019-07, https://doi.org/10.15138/wkgj-f215

Feldman, D. R., Collins, W. D., Pincus, R., Huang, X., & Chen, X. (2014). Far-infrared surface emissivity and climate. Proceedings of the National Academy of Sciences of the United States of America, 111(46), 16,297–16,302. https://doi.org/10.1073/pnas.1413640111

GLOBE Task Team, Hastings, D. A., Dunbar, P. K., Elphingstone, G. M., Bootz, M., Murakami, H.,…MacDonald, J. S. (1999). The Global Land One kilometer Base Elevation (GLOBE) digital elevation model, Version 1.0. National Oceanic and Atmospheric Administration, National Geophysical Data Center, 325 Broadway, Boulder, CO. Digital data base on the World Wide Web. Retrieved from http://www.ngdc.noaa. gov/mgg/topo/globe.html and CDROMs.

Green, P., S. Newman, R. Beeby, J. Murray, J. Pickering and J. Harries (2012), Recent advances in measurement of the water vapour continuum in the far-IR spectral region. Phil. Trans. R. Soc. A, 370, 2637-2655

Harries, J., Carli, B., Rizzi, R., Serio, C., Mlynczak, M., Palchetti, L.,…Masiello, G. (2008). The far-infrared Earth. Reviews of Geophysics, 46, RG4004.Hori, M., Aoki, T., Tanikawa, T., Motoyoshi, H., Hachikubo, A., Sugiura, K., … Takahashi, F. (2006). In-situ measured spectral directional emissivity of snow and ice in the 8–14 μm atmospheric window. Remote Sensing of Environment, 100(4), 486–502. https://doi.org/10.1016/j.rse.2005.11.001

Huang, X., X. Chen, M. Flanner, P. Yang, D. Feldman and C. Kuo (2018). Improved representation of surface spectral emissivity in a global climate model and its impact on simulated climate, *J. Clim*., 31, 3711-3727

Knuteson, R., Best, F., DeSlover, D., Osborne, B., Revercomb, H., & Smith,W. Sr. (2004). Infrared land surface remote sensing using high spectral resolution aircraft observations. Advances in Space Research, 33(7), 1114–1119. https://doi.org/10.1016/S0273 1177(03)00752-X

Kuo, C., D. Feldman, X. Huang, M. Flanner, P. Yang and X. Chen (2018). Time-dependent cryospheric longwave surface emissivity feedback in the Community Earth System Model, *J. Geophys. Res*., 123, 789-813

Li, Z-L, Wu, H., Wang, N., Qiu, S., Sobrino, J., Wan, Z.,… Yan, G. (2013). Land surface emissivity retrieval from satellite data. *International Journal of Remote Sensing*, 34, 3084-3127

Martin, D. H., & Puplett, E. (1969). Polarised interferometric spectrometry for the millimeter and submillimeter spectrum. Infrared Physics, 10, 105–1097.

Miloshevich, L., Vomel, H., Whiteman, D., Leblanc, T. (2009). Accuracy assessment and correction of Vaisala RS92 radiosonde water vapour measurements, J. Geophys. Res. Atmos., **114**, D11305. https://doi.org/10.1029/2008JD011565.

Mlawer, E., Turner, D., Paine, S., Palchetti, L., Bianchini, G., Payne. V., Cady-Pereira, K., Pernak, R…. (2019) Analysis of water vapor absorption in the far-infrared and submillimetre regions using surface radiometric measurments from extremely dry locations, J. Geophys. Res. Atmos., **124**/14, 8134-8160, DOI 10.1029/2018JD029508.

Newman, S. M., Smith, J. A., Glew, M. D., Rogers, S. M., & Taylor, J. P. (2005). Temperature and salinity dependence of sea surface emissivity inthe thermal infrared. Quarterly Journal of the Royal Meteorological Society, 131(610), 2539–2557. https://doi.org/10.1256/qj.04.150

Ostby, T., T. Schuler and S. Westermann (2014). Severe cloud contamination of MODIS Land Surface Temperatures over an Arctic ice cap, Svalbard, Rem. Sens. Env., 142, 95-102

Palchetti, L., Olivieri, M., Pompei, C., Labate, D., Brindley, H., Di Natale, G., Bianchini, G. and the FORUM team (2016), The Far Infrared FTS for the FORUM Mission, in Light, Energy and

the Environment, OSA Technical Digest (online) (Optical Society of America, 2016), paper FTu3C.1.

Palchetti, L., et al. (2020) FORUM: Unique far-infrared satellite observations to understand how Earth radiates energy to space. Accepted for publication in BAMS.

Rathke, C., Fisher, J., Neshyba, S. and Shupe, M (2002) Improving IR cloud phase determination with 20 μm spectral observation, Geophys. Res. Lett., **29**, 501-504.

Sweeney, C., Karion, A., Wolter, S., Newberger, T., Guenther, D., Higgs, J., Andrews, A., Lang, P.,… Tans, P. (2015). Seasonal climatology of CO_2 across North America from aircraft measurements in the NOAA/ESRL Global Greenhouse Gas Reference Network. J. Geophys. Res. Atmos., **120**, 5155-5190, doi:10.1002/2014jD022591.

Vance, A. K., Abel, S. J., Cotton, R. J., & Woolley, A. M. (2015). Performance of WVSS-II hygrometers on the FAAM research aircraft. Atmospheric Measurement Techniques, 8(3), 1617–1625. https://doi.org/10.5194/amt-8-1617-2015

Vomel, H., T. Hock, N. Potts, M. Goodstein, C. Arendt, L. Tudor and K. Young (2016) 'Overview of NCAR Dropsonde technologies for targeted observations in severe systems and for research', Technical Conference on Meteorological and Environmental Instruments and Methods of Observation, September 27-30, Madrid, Spain.
Wan, Z., D. Ng, and J. Dozier, 1994: Spectral emissivity measurements of land-surface materials and related radiative transfer simulations. *Adv. Space Res.*, **14**, 91–94.

Wang, D., Prigent, C., Kilic, L., Fox, S., Harlow, C., Jimenez, C., Aires, F., Grassotti, F. and Karbou, F. (2017) Surface Emissivity at Microwave to Millimeter Waves overs Polar Regions: Parameterization and Evaluation with Aircraft Experiments. J. Atmos. Oceanic Technol., **34**, 1039-1059, https://doi.org/10.1175/JTECH-D-16-0188.1.

Wilson, S. H. S., Atkinson, N. C., & Smith, J. A. (1999). The development of an airborne infrared interferometer for meteorological sounding studies. Journal of Atmospheric and Oceanic Technology, 16(12), 1912–1927. https://doi.org/10.1175/1520-0426(1999)016%3C1912:TDOAAI%3E2.0.CO;2

Figure 1. (a) Inset: B898 flight track and surface elevation over Greenland (surface elevation from GLOBE, 1999). Black box indicates the region highlighted in the main image; Main Image: Dropsonde release locations shown as blue triangles, the black diamonds represent the start of TAFTS nadir cycles with the black lines indicating the along track length of the nadir view. The white cross indicates the position of the Summit ground station and the white square the location of the low level emissivity measurements of B17. (b) Similar plot projected on the 13:20 UTC MODIS (Terra) 11 μm brightness temperature background. (c) The along flight track a-priori surface temperature (black stars) derived from ARIES assuming a surface emissivity of 0.995. In red are the spatially coincident MODIS (Terra) 11 μm brightness temperatures from 13:20 UTC. The green diamonds show the closest 12:00 UTC ERA interim surface temperature for cycles 8 to 10. The black horizontal bars above each cycle indicate the timing of the 50 second TAFTS nadir views. The blue line represents the surface elevation determined from the aircraft altitude and lidar return signal, the apparent rapid variation in surface elevation around 13.99 UTC is an artifact caused by the aircraft turn after cycle 9

Table 1. Timing and location details for each TAFTS nadir cycle. The mean and range in surface elevation during each cycle is determined from the lidar return signal. The total column water vapour for

cycles 8, 9 and 10 is obtained from dropsonde 11 allowing for the variation in surface elevation between the cycles.

Figure 2. (A) Temperature profiles for dropsondes 10 (purple) and 11 (green) released from the aircraft at a pressure level of 287 mbar, and two sonde releases from Summit camp at 11:19 (black) and 14:52 UTC (red). (B) Temperature difference between dropsonde 10 and the two sondes and dropsonde 11. ERA-interim data is used to extend dropsonde 11 profiles to lower pressure levels. Panels (C and D) show the equivalent water vapour profiles and differences. Panels E – G show the ERA-5 total column water vapour at 11:00 UTC (E), 14:00 UTC (F) and 15:00 UTC (G), approximately corresponding to the release times of the various sondes.

Figure 3. Upper panel: Typical ARIES nadir observation from cycle 10. Over-plotted in orange is the atmospheric transmission derived from LBLRTM using the relevant dropsonde interpolated atmospheric profile. The red and blue curves show ice and snow emissivity, respectively, as given by UCSB, Mammoth Lakes SNOW_1 and ICE01 (Wan *et al*., 1994). The central thick green line indicates the wavenumber band used to derive the a-priori surface temperature estimate and the light green lines to either side indicate the regions covered by the CO_2 P and R branches used in the surface temperature retrieval. Lower panel: The ARIES noise equivalent spectral radiance, 1 RU= $1mW\ m^{-2}\ sr^{-1}\ (cm^{-1})^{-1}$.

Figure 4. Panels a-c: Examples of the standard deviation in retrieved emissivity over the P and R branch (see text for details). Panel d shows the difference in the surface temperature retrievals between the two branches plotted against the a-priori surface brightness temperature. Panel e: Retrieved surface temperature for each ARIES average spectrum relative to the start of individual scan cycles (Cycle 10 ARIES scans are off-set in time by 10 s as these data were acquired just prior to TAFTS data). The horizontal bars indicate the ARIES spectra that have coincident TAFTS measurements, colour coded according to cycle.

Figure 5: Impact of uncertainties in retrieved emissivity due to changes in atmospheric state, path length and spectroscopy for cycle 8, expressed as the difference in retrieved emissivity, Δε, between the perturbed and the control case. Note that Δε over the TAFTS range is an order of magnitude larger than over the ARIES range.

Figure 6: MIR surface emissivities retrieved from the 5 s average ARIES radiance spectra colocated with TAFTS spectra. Panels a and b correspond to cycle 8, Panels c-f to cycle 9 and g and h to cycle 10. Uncertainties resulting from the surface temperature retrievals are shown in blue.The black bars indicate the standard deviation in the retreived emissivity within each 10 cm^{-1} band. The emissivities derived by B17 are shown in green in panels g and h. Orange lines show the simulated transmission of the layer between the surface and the FAAM aircraft.

Figure 7. TAFTS nadir radiances for selected scans and cycles. The panel on the left are radiances acquired from TAFTS longwave channel and the panel on the right from TAFTS shortwave channel. Shown in red is the associated atmospheric transmission, derived from LBLRTM, for cycle 10. Lower panels show the noise equivalent spectral radiance, 1 RU = $1mW\ m^{-2}\ sr^{-1}\ (cm^{-1})^{-1}$.

Figure 8: Retrieved FIR emissivity from TAFTS for cycles 8-10. The emissivity is averaged over discrete wavenumber bands coincident with regions of high transmission, shown in blue. The black error bars indicate the uncertainty associated with TAFTS calibration, instrument noise and the variation in the emissivity retrievals within each micro-window. The vertical blue bars to the right indicts the uncertainty in the retrieved emissivity associated with $\Box T_s$. Plotted in green, in panels g and h, are the retrieved emissivities and their corresponding uncertainties from B17.

Figure 9. Averaged emissivity covering both the TAFTS and ARIES spectral range for each of the 3 cycles
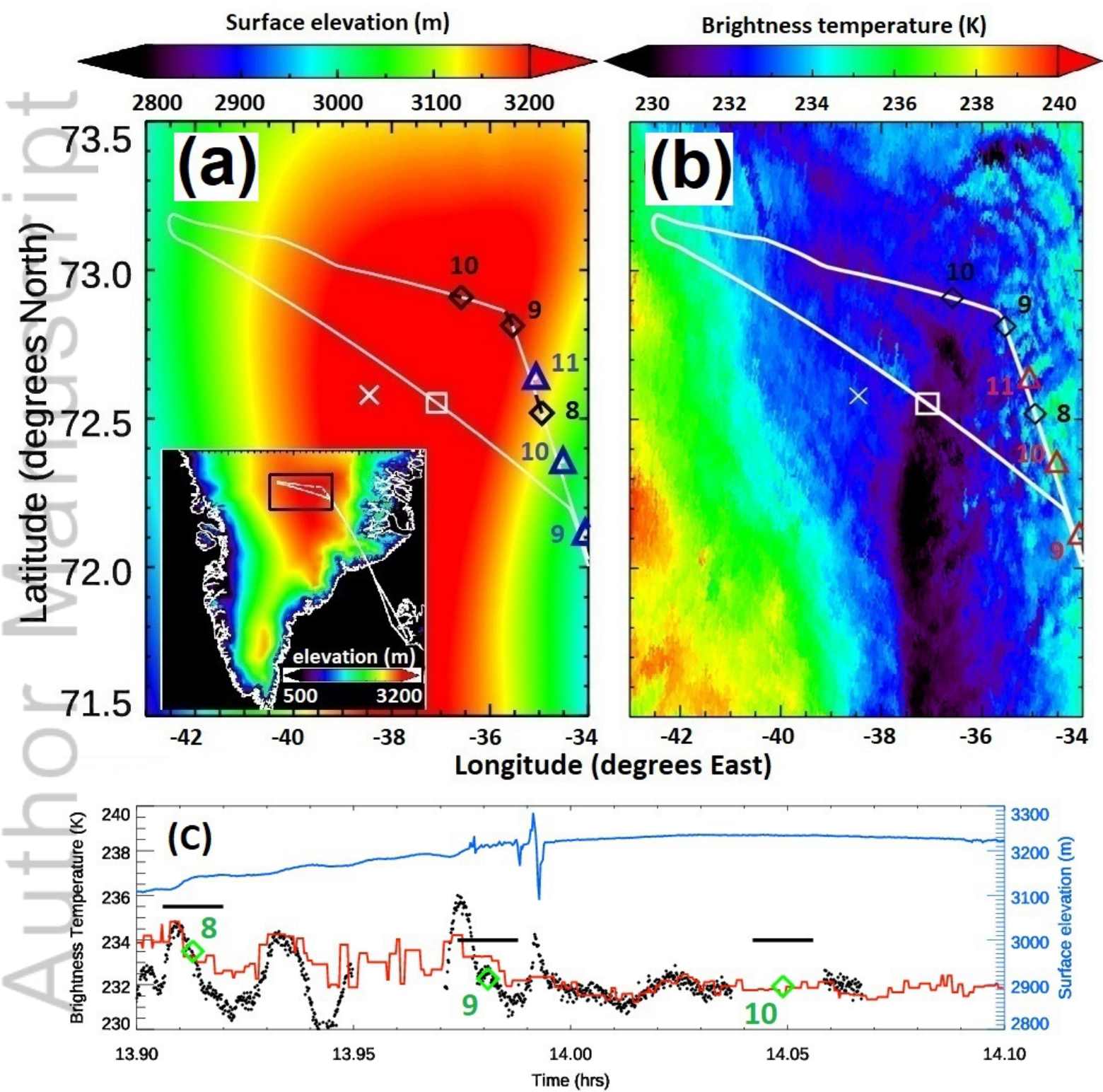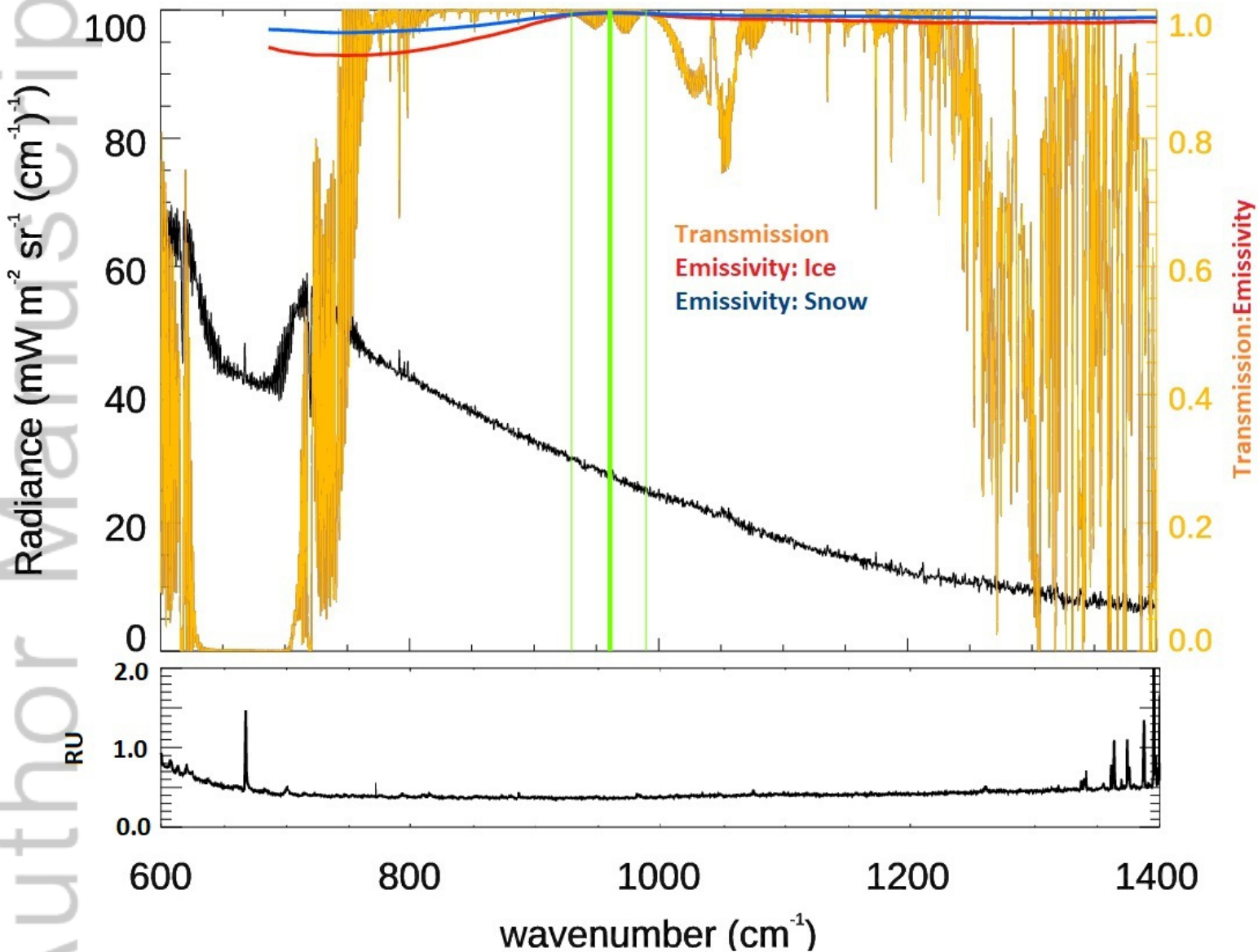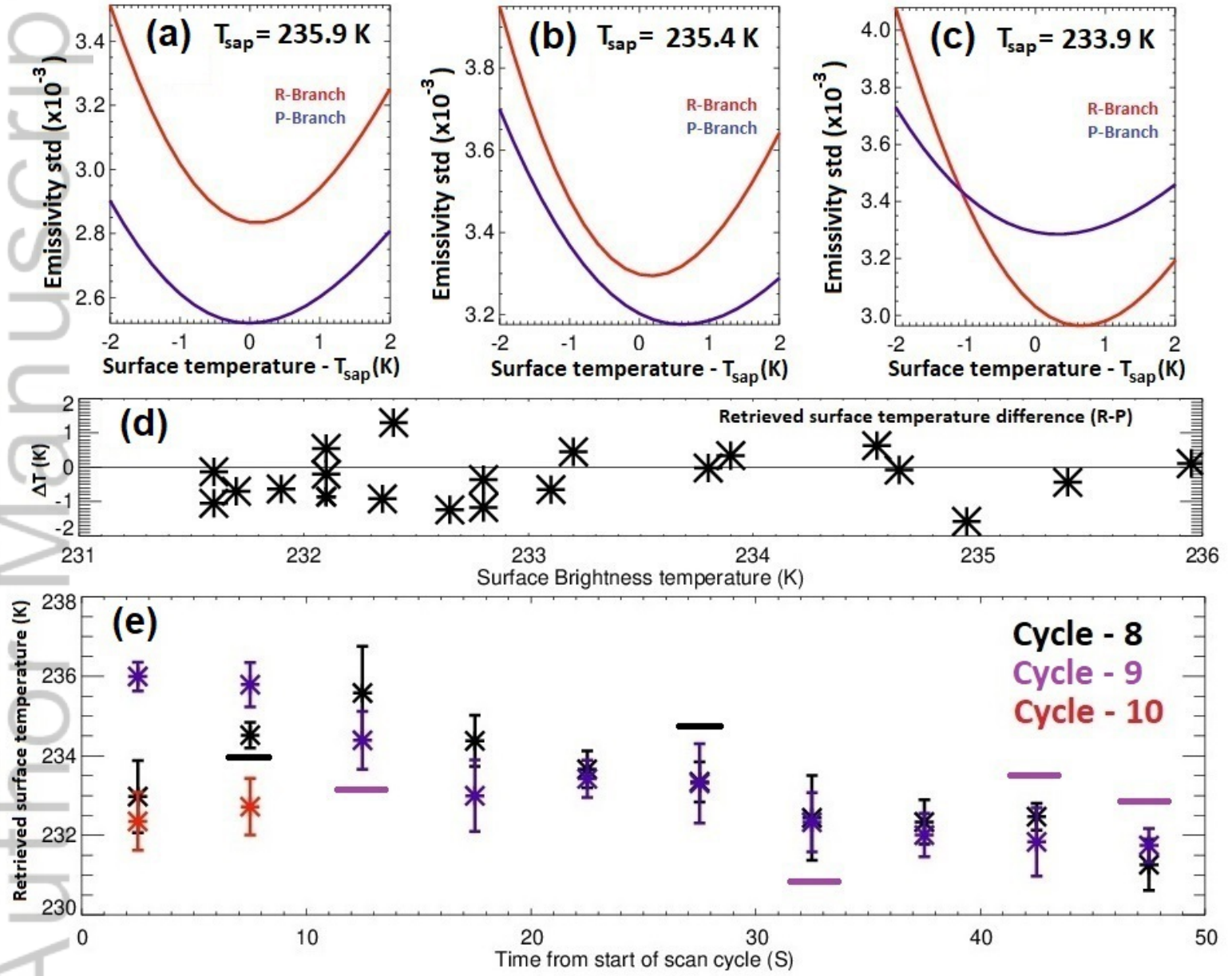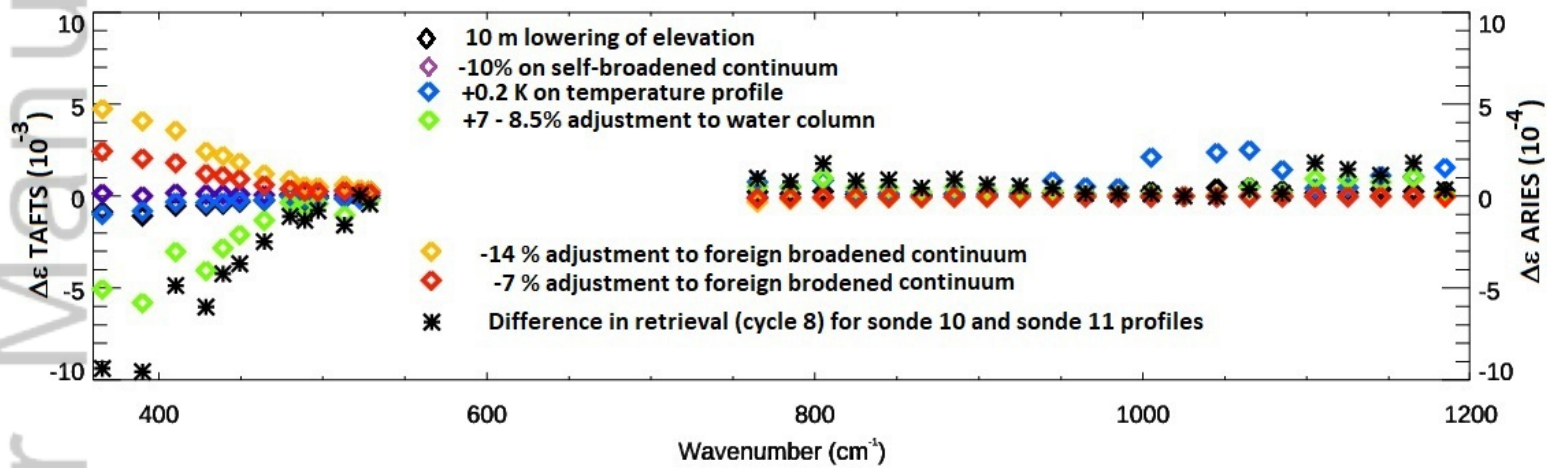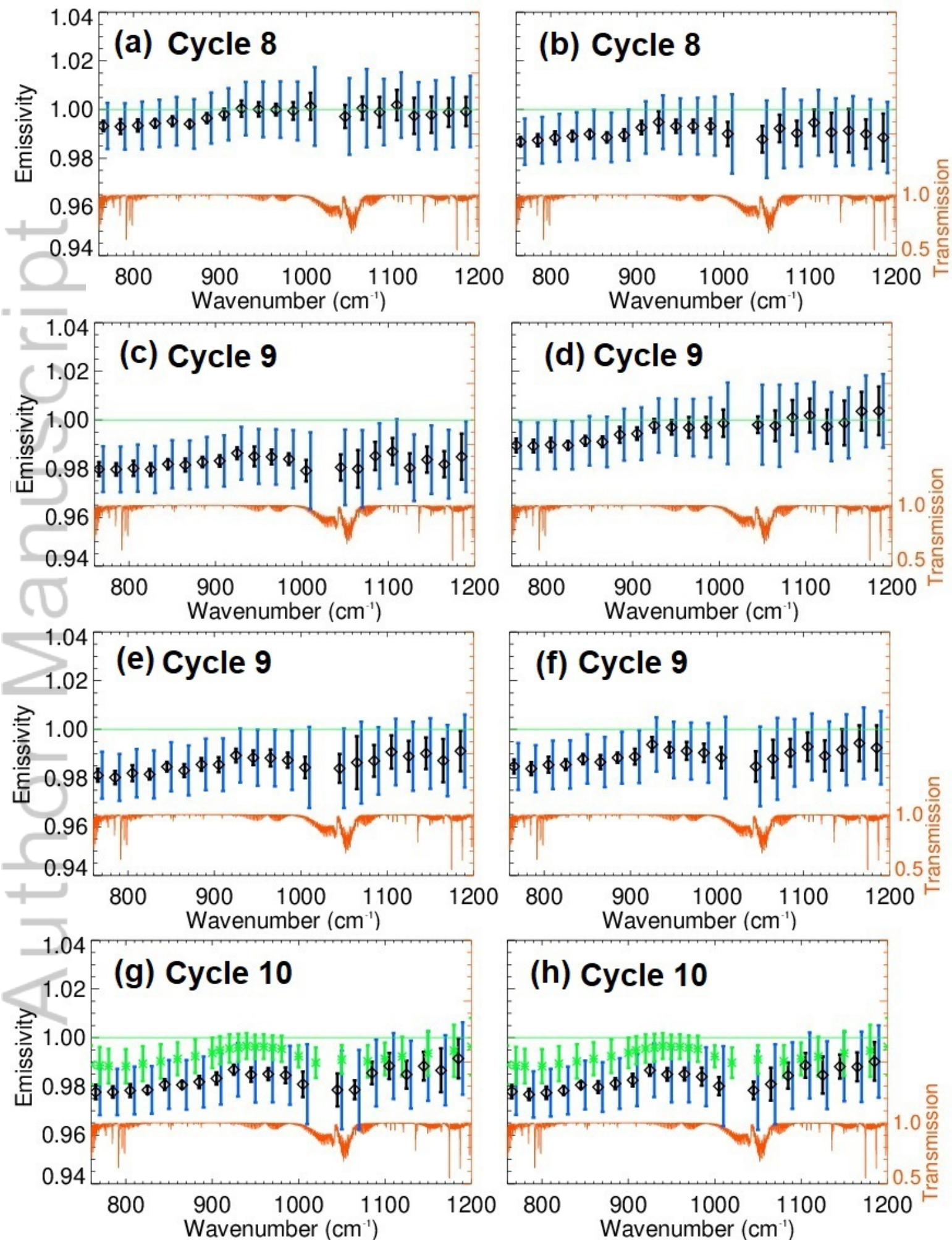
JGRD_56608_2020JD033672-f01-z-.jpg
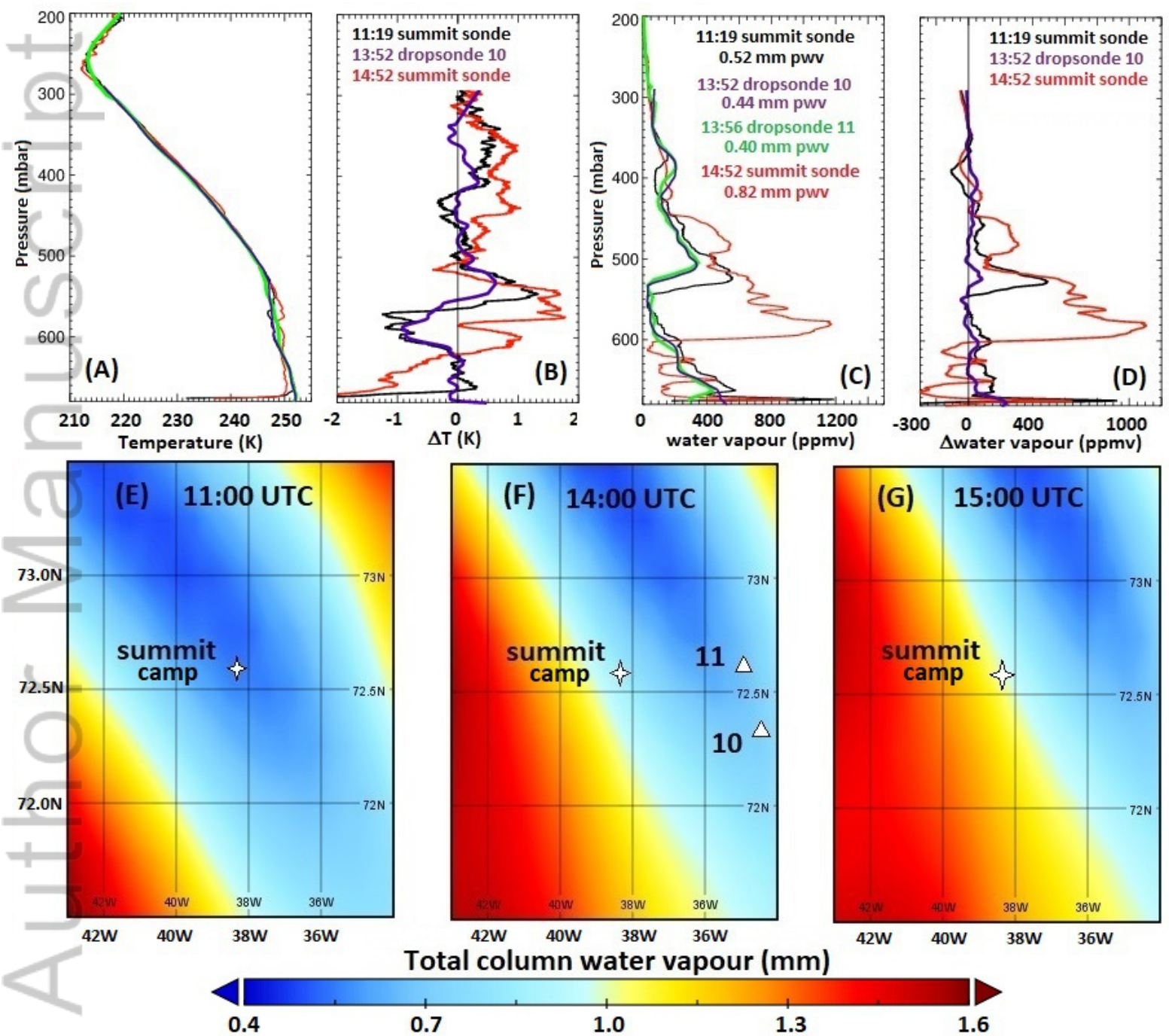
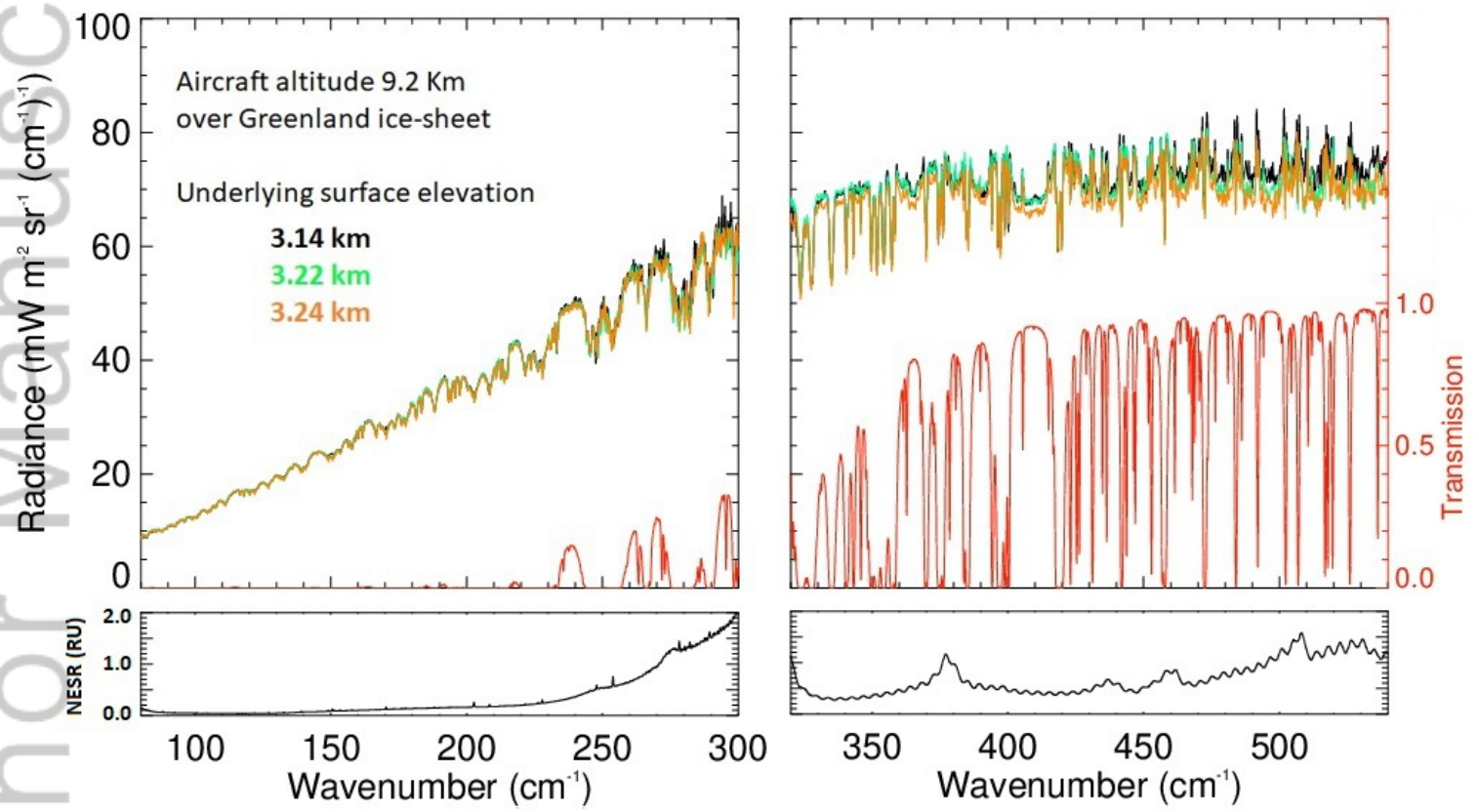JGRD_56608_2020JD033672-f02-z-.jpg

JGRD_56608_2020JD033672-f03-z-.jpg

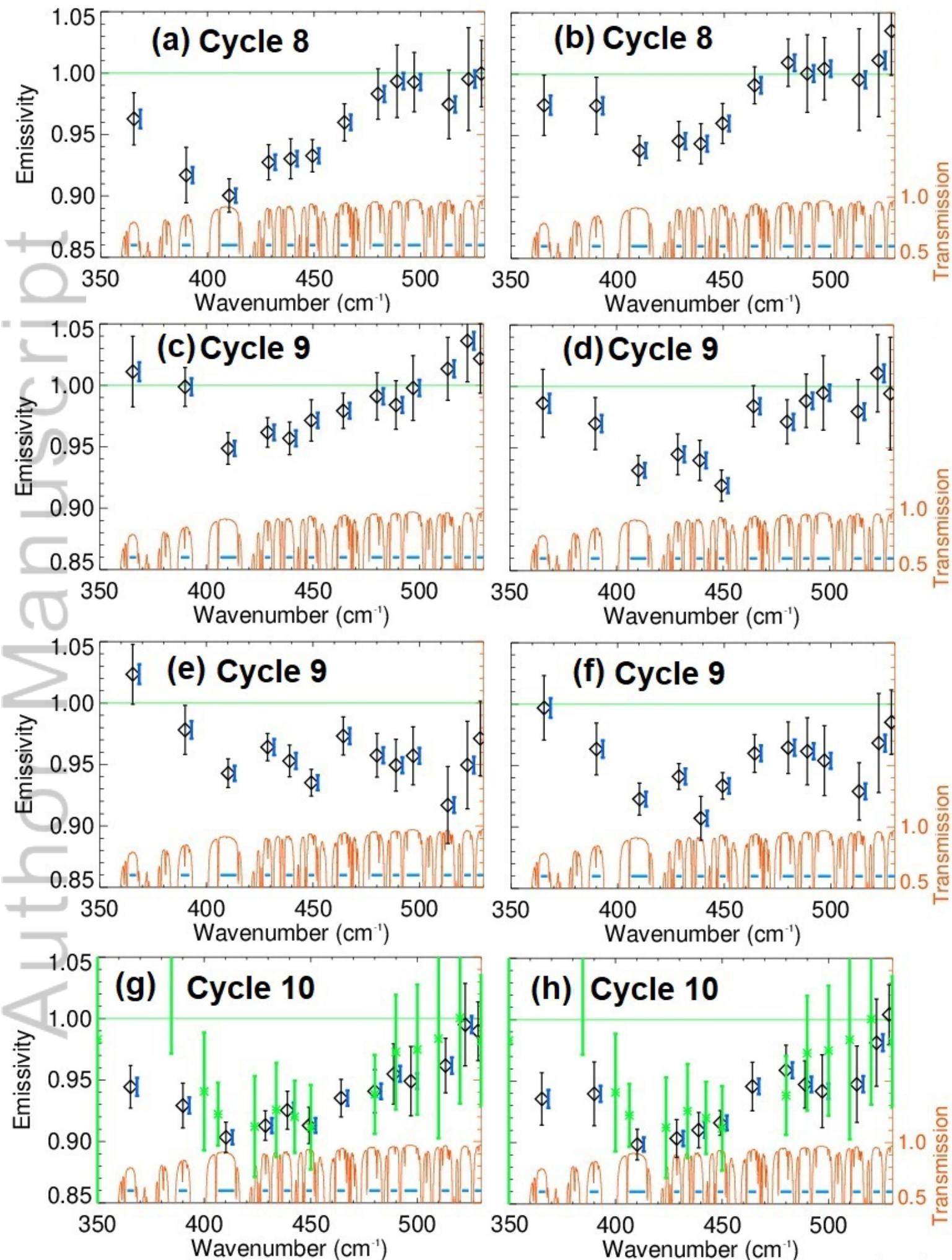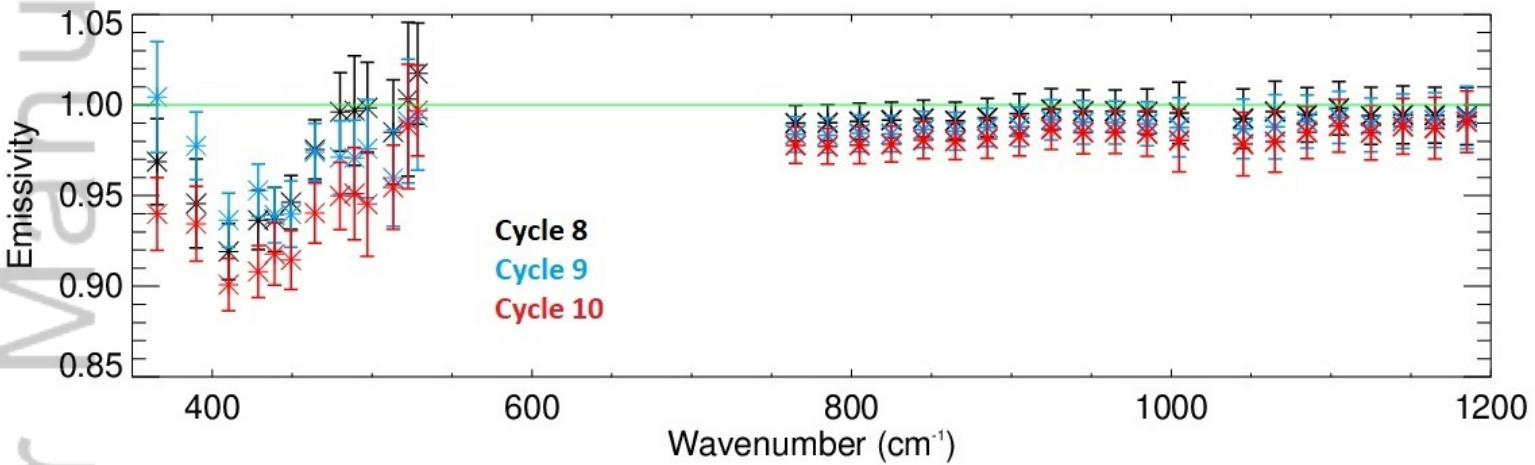JGRD_56608_2020JD033672-f04-z-.jpg

JGRD_56608_2020JD033672-f05-z-.jpg

JGRD_56608_2020JD033672-f07-z-.jpg

JGRD_56608_2020JD033672-f09-z-.jpg